49th AIAA Aerospace Sciences Meeting including the New Horizons Forum and Aerospace Exposition
4 - 7 January 2011, Orlando, Florida
AIAA 2011-1313

A Scaling Parameter for the Thrust Generation of Flapping Flexible Wings

Chang-kwon Kang*, Hikaru Aono†, Carlos S., Cesnik‡,
Department of Aerospace Engineering, University of Michigan, Ann Arbor, MI, 48109

and

Wei Shyy§
Department of Aerospace Engineering, University of Michigan, Ann Arbor, MI, 48109
Department of Mechanical Engineering, Hong Kong University of Science and Technology, Kowloon, Hong Kong

Thrust generation and scaling parameters for flapping flexible wings are investigated using an integrated framework of computational fluid dynamics and structural dynamics solvers. To explore the influences of the density ratio and the effective stiffness on the thrust generation, surrogate models have been generated for a flapping thin isotropic flat Zimmerman wing in still air at $Re = 1.5\times10^3$. Time averaged thrust, bending angle, and twist show qualitatively similar behavior and increased with higher ratio between the density ratio and effective stiffness. Flexibility-induced twisting in the wing promotes the thrust generation. To further investigate the flexibility-induced thrust enhancement, plunging chordwise flexible airfoils in forward flight at $Re = 9.0\times10^3$ in water are considered. Time averaged thrust increases with larger airfoil thickness, however the thinnest airfoil responded with degradation in performance when motion frequency becomes high. Finally, unified scaling parameters are proposed based on properly normalized governing equations and give a priori order of magnitude estimation of the time averaged thrust and the degree of fluid-structure coupling. The results show that these scaling parameters, given as combinations of the wing geometry, structural properties, and the motion amplitude and frequency, can be applied for both cases with different motion type, Reynolds number, and the fluid medium.

Nomenclature

AR	= aspect ratio, b^2/S	[1]
C_L	= lift coefficient, $F_1/\left(1/2\rho_f U_{\text{ref}}^2 S\right)$	[1]
c_m	= mean chord length	[m]
C_T	= thrust coefficient, $-F_2/\left(1/2\rho_f U_{\text{ref}}^2 S\right)$	[1]
$\boldsymbol{d}_\Gamma^{n+1}$	= displacement vector of the fluid-structure interface Γ	[m]
$\tilde{\boldsymbol{d}}_\Gamma^{n+1}$	= displacement output from the structural solver at Γ	[m]
E	= Young's modulus of material	[Pa]
f	= motion frequency	[1/s]
f_n	= natural frequency of the structure	[1/s]
F_i	= fluid force vector	[N]
h_a	= plunging amplitude	[m]

* Graduate Student Research Assistant, Department of Aerospace Engineering, University of Michigan, AIAA Student Member
† Post-doctoral Research Fellow, Department of Aerospace Engineering, University of Michigan, AIAA Member
‡ Professor, Department of Aerospace Engineering, University of Michigan, AIAA Associate Fellow
§ Clarence L. "Kelly" Johnson Collegiate Professor, Department of Aerospace Engineering, University of Michigan; currently, Provost & Chair Professor, Department of Mechanical Engineering, Hong Kong University of Science and Technology, AIAA Fellow

h_s	= thickness of the wing	[m]
k	= reduced frequency, $\pi f c_m / U_{\text{ref}}$	[1]
N_{FSI}	= number of fluid-structure interaction subiterations	[1]
N_s	= number of training points	[1]
p	= pressure	[Pa]
$\boldsymbol{r}$	= displacement residual at Γ, $\boldsymbol{r} = \tilde{\boldsymbol{d}} - \boldsymbol{d}$	[m]
R	= semi-span	[m]
Re	= Reynolds number, $\rho_f U_{\text{ref}} c_m / \mu$	[1]
t	= time	[s]
S	= wing planform area	[m^2]
Sr	= Strouhal number, $Sr = 2St$	[1]
St	= Strouhal number, plunging: $f h_a / U_{\text{ref}}$	[1]
	flapping: $f \phi_a R / U_{\text{ref}}$	[1]
T	= thrust	[N]
U_{ref}	= reference velocity: U_{tip} for hover, U_∞ for forward flight	[m/s]
U_{tip}	= time averaged wing tip velocity, $2R\Phi f$	[m/s]
U_∞	= free stream velocity	[m/s]
u_i	= velocity vector	[m/s]
x_i	= position vector	[m]
α	= angle of attack	[degree or radian]
Γ	= fluid-structure interface	[1]
ϵ	= convergence criteria for the fluid-structure coupling	[1]
γ	= thrust shape factor	[1]
γ_{thrust}	= corrected thrust shape factor	[1]
γ_{FSI}	= Fluid-Structure Interaction shape factor	[1]
ν	= Poisson's ratio	[1]
μ	= dynamic viscosity of fluid	[Pa s]
Π_0	= effective inertia, $\rho^* h_s^* (k/\pi)^2$	[1]
Π_1	= effective stiffness, plate: $E h_s^3 / \left[12(1-\nu^2)\rho_f U_{\text{ref}}^2 c_m^3\right]$	[1]
	beam: $E h_s^3 / \left[12 \rho_f U_{\text{ref}}^2 c_m^3\right]$	[1]
ρ^*	= density ratio, ρ_s / ρ_f	[1]
ρ_f	= density of fluid	[kg m^{-3}]
ρ_s	= density of structure	[kg m^{-3}]
ϕ	= flapping angle	[degree or radian]
ϕ_a	= flapping amplitude	[degree or radian]
ω	= motion angular frequency	[1/s]
ω_i	= relaxation factor for fluid-structure interface	[1]
ω_n	= natural frequency of the fluid-structure system	[1/s]
$\mathcal{N}_{ei}$	= Elastoinertial number = $\rho_f h_s h_a f^2 c_m^3 / (E h_s^3)$	[1]
$(\cdot)^*$	= normalized variable	[1]
$<\cdot>$	= time averaged variable: $f \int_0^{1/f} (\cdot)\, dt$	[1]

I. Introduction

The flapping mechanisms inherent to the biological flyers, such as insects and birds, have inspired the most exotic dreams, ever since the history of human beings, from Daedalus and Icarus in the Greek mythology, via Leonardo Da Vinci's ornithopter, to a recent successfully sustained human powered flapping flight[1] at human scales. At smaller scales of 15 cm or less micro air vehicles (MAV) are of great interest in remote sensing and information gathering capabilities both in military as well in civilian applications. Smaller sizes and lower flight speeds lead to lower Reynolds numbers and higher sensitivity to wind gust effects than for the conventional airplanes. Moreover, wing structures have high flexibilities to promote favorable flight performance[2-5]. Consequently, design of a high performance and robust MAV become a highly nonlinear complex process that requires solid understanding of aerodynamics, structural dynamics, control, and interactions of these.

The physics exhibited by the biological flyers have potentials to be applied in the MAV design[2-5]. Unsteady aerodynamic mechanisms such as the generation of leading-edge vortex (LEV), wing-wake interaction, and three-dimensional flow features, such as tip vortex-vortex interactions, all contribute significantly to control the aerodynamic force generation[3]. Another remarkable mechanism that the biological flyers seem to be using is the wing flexibility. Combes and Daniel[6] have shown that a variety of insects poses anisotropy in their wing structures. The spanwise flexural rigidity was 1 or 2 orders of magnitudes larger than the chordwise flexural rigidity. Experimental[7,8], analytical[9], and numerical studies[10-12] have presented that the chordwise flexibility affects the redistribution of the resulting aerodynamic forces in the lift and the thrust directions. The airfoil shape undergoes deformation leading to effective geometry such as camber variation, the airfoil motion changes the effective angle of attack, and combined with the pitching angle the direction of the net force can be changed in favor of the thrust generation. For a range of spanwise flexibilities, the thrust enhancement was seen when the wing motion was in phase with the variation of the airfoil deformation in spanwise direction[13,14]. The fluid-structure density ratio also affects the thrust generation: Zhu[16] showed numerically that the thrust and the propulsive efficiencies increased for a plunging chordwise flexible airfoil in water than immersed in air. Hence it is seen that the flexibility, including the density ratio, can be utilized to control resulting aerodynamic forces. More recently, Eldredge *et al.*[17] found that a hovering flexible wing allows for lift generation even when the leading edge remains nearly vertical, as the wing passively deflects to create an effectively smaller angle of attack, similar to the wing passive pitching mechanism recently identified for rigid wings[10].

Different level of fidelity and diverse numerical algorithms, depending on the objective of the study and accuracy and cost of the computations, can be incorporated into a numerical framework of flexible flapping wing simulations. High-fidelity framework can be used to evince the rich and complex physics behind a flexible flapping wing aerodynamics, while a low-fidelity model can be used for quick yet reliable design optimization of a complex and multi-dimensional design space. The aeroelastic coupling can be based on a time-domain partitioned process where the interaction between the fluid and the solid fields occurs at a shared boundary iteratively at a given time step. An advantage is that for the solutions of both fields, which are described by different nonlinear partial differential equations, well-established solvers can be used. Tang *et al.*[18], Chimakurti *et al.*[14, 19], and Aono *et al.*[20, 21] have coupled an in-house structured finite volume Navier-Stokes solver to a beam model[18], a commercial nonlinear finite-element solver, MSC.Marc[14, 22], a geometrically nonlinear active beam solver[14], and a co-rotational shell finite element solver[3,19-21] , respectively. More recently, Gordnier *et al.*[23] coupled an in-house high-order Navier-Stokes solver to a geometrically nonlinear active beam solver, McClung *et al.*[24] developed the OVERFLOW Navier-Stokes solver to a modal representation of two-dimensional beam, Stanford *et al.*[25] showed a two-dimensional quasi-steady blade element model to a nonlinear co-rotational beam model, and Gogulapati *et al.*[26] presented an approximate aerodynamic model to a commercial nonlinear finite-element solver, MSC.Marc. Another interest regarding the Fluid-Structure-Interaction (FSI)-coupling using the partitioned methods is the stability and the acceleration of the synchronization of the coupled solutions. Light structure (ex. parachute) in air, or wing made of aluminum in water lead to a system with comparable densities and can cause numerical instabilities[27]. If the density ratio between the fluid and the structure approaches unity the added mass effects become important and either monolithic solver or strongly, or tightly coupled implicit scheme with sub-iterations is necessary[28-30]. Coupling strategies for tightly coupled system have been investigated for parachute aeroelasticity and hemodynamics, however the FSI-coupling stability needs yet to be addressed.

Scaling parameters resulting from dimensional analysis and by non-dimensionalizing the governing equations by relevant physical variables, often give qualitative characteristics of the model as well as the requirement for dynamic similarity of the flow[31]. Depending on the type of the model and the governing equations the resulting set of scaling parameters may vary. For example, Shyy *et al.*[10] have considered the Navier-Stokes equation with out-of-plane motion of isotropic plate, Ishihara *et al.*[11], the Navier-Stokes equation and the wing structure as a linear isotropic elastic body to study the flexibility effect on wing pitch changes in dipteran flapping flight, and Lentink and Dickinson[32] transformed the Navier-Stokes equation in the wing-fitted frame of reference and focused on the rotational motion of the wing. Thiria and Godoy-Diana[33] have measured the thrust and the propulsive efficiency of a self-propelled flapping flyer in air. Since the density ratio is high the elastic deformation of the wing is only balanced by the wing inertia. They introduce the elastoinertial number to define the ratio between the inertial forces and the elastic restoring forces and show that the measured thrust scales with the elastoinertial number. Still, the parameter-space involving the scaling parameters for the fluid-structure interaction needs to be mapped out in a systematic fashion to understand the role of flexibility on the aerodynamic force generations and the stability of coupled system.

The objective of the current study is twofold. Firstly, a surrogate model will be constructed using the structural properties the effective stiffness and the density ratios as design variables to assess the parametric dependence on the

thrust generation for a homogeneous isotropic flapping wing at Reynolds number (Re) of 1.5×10^3 and reduced frequency (k) of 0.56. Secondly, scaling parameters that estimate the thrust and the degree of FSI-coupling for a flapping flexible wing will be identified. Identifying these scaling parameters can lead to a priori order of magnitude estimation of the thrust and the required computational resources to simulate often expensive computations.

The numerical framework to simulate a moving flexible wing is developed based on coupled two standalone solvers. The fluid solver is a parallelized finite-volume pressure-based Navier-Stokes equation solver and the structural dynamics solver uses the finite element method with either a combination of an optimal membrane element and a discrete Kirchhoff triangle bending plate element in co-rotational formulation[19, 21] or a linear beam element. In the tightly coupled fluid-structure interaction interface the equilibrium condition on the wing surface are communicated to each solver using either the radial basis function[33] interpolation or the bilinear interpolation. The radial basis function interpolation[21, 33] is also applied to remesh the grid used in the fluid solver to update for the wing movement and deformations. To efficiently organize the obtained numerical solutions and to accurately interpolate the nonlinear objective functions in the design space the surrogate model approach will be used. A surrogate model offers a versatile and efficient way of parametrizing and categorizing the results of expensive computations. After the optimally choosing the training points, surrogate model are constructed minimizing the errors at off design points. This approach has shown to be valuable for wide range of applications involved with plasma actuators[35], Lithium-Ion battery limitations[36], and rigid wing flapping aerodynamics[37].

The outline of this paper is as follows. Firstly, the numerical framework for flexible flapping wings will be described. Secondly, dimensional analysis will be performed based on the governing equations for the fluid and the solid, given the wing kinematics and the structural properties, in order to identify the key non-dimensional parameters representing the flexible flapping wing aerodynamics. Thirdly, surrogate models for a flapping wing model in air made of homogeneous isotropic materials will be constructed based on the variations of effective stiffness and density ratio to relate the thrust generation to the wing deformations. Fourthly, chordwise flexible airfoil in forward flight in water will be considered for different thickness ratios and motion frequencies. Finally, unified scaling parameters are presented that estimate the time averaged thrust and the degree of fluid-structure coupling for all cases considered.

II. Methodology

A. Numerical Models

1. Computational Fluid Dynamics

The governing equations for the fluids are the three-dimensional Navier-Stokes equations with constant density and viscosity shown in Eqs. (1) and (2),

$$\frac{\partial u_j}{\partial x_j} = 0, \tag{1}$$

$$\frac{\partial u_i}{\partial t} + \frac{\partial u_j u_i}{\partial x_j} = -\frac{1}{\rho_f}\frac{\partial p}{\partial x_i} + \mu\frac{\partial}{\partial x_j}\left(\frac{\partial u_i}{\partial x_j}\right), \tag{2}$$

where u_i is the velocity vector, x_i is the position vector, t is the time, p is the pressure, ρ_f is the fluid density, and μ the viscosity of the fluid. Eqs (1) and (2) are solved with an in-house code[38, 39], which is a three-dimensional, unstructured, pressure-based finite volume solver written in the LOCI-framework[40]. It employs implicit first or second order time stepping and treats the convection terms using the second order upwind-type scheme[41, 42], and the pressure and viscous terms using second order schemes[41, 42]. The system of equations resulting from the linearized momentum equations are handled with the symmetric Gauss-Seidel solver. The pressure correction equation[43] is solved with either the GMRES linear solver with Jacobi preconditions provided by PETSc[44] or the BoomerAMG linear solver provided by HYPRE[45]. The LOCI is by design rule-based highly parallelizable framework for finite volume methods, see Luke and George[40] for a more detailed discussion on rule-based software. The geometric conservation law[46], a necessary consideration in domains with moving boundaries, is satisfied[47]. The mesh deformations are realized using radial basis function (RBF) interpolations[34].

2. Structural Dynamics

Two structural dynamics solvers of two-level fidelities have been incorporated. For linear analysis of a beamlike flat plate an Euler-Bernoulli beam model has been incorporated to solve Eq. (3),

$$\rho_s h_s \frac{\partial^2 w_3}{\partial t^2} + \frac{E h_s^3}{12} \frac{\partial^4 w_3}{\partial x_1^4} = f, \tag{3}$$

where w_3 is the displacement in the x_3 direction, ρ_s the density of the plate, h_s the thickness of the plate, E the Young's modulus of the material, ν the Poisson's ratio of the material, and f the distributed transverse load on the beam per unit span.

The nonlinear structural dynamics are solved using a flexible multi-body type finite element analysis of a flapping wing using triangular shell elements. The rigid-body motions are prescribed in the global frame of reference in addition to a co-rotational framework to account for the geometric nonlinearities. By applying the co-rotational frame transformations the motion of an element is decomposed into the rigid-body motion part and the pure deformation part. By using the linear elasticity theory for the latter part, the co-rotational formulation can efficiently solve for the structural dynamics with small strains, yet large rotations. A linear combination of an optimal membrane element and a discrete Kirchhoff triangle plate bending element is employed for the elastic stiffness of a shell element[48]. Full details of this algorithm are described in Refs. [19] and [48]. The out-of-plane displacement of a linear isotropic plate is given by Eq (4),

$$\rho_s h_s \frac{\partial^2 w_3}{\partial t^2} + \frac{E h_s^3}{12(1-\nu^2)} \left(\frac{\partial^4 w_3}{\partial x_1^4} + 2 \frac{\partial^4 w_3}{\partial x_1^2 \partial x_2^2} + \frac{\partial^4 w_3}{\partial x_2^4} \right) = f, \tag{4}$$

where ν is the Poisson's ratio of the material, and f the distributed transverse load on the plate.

3. Fluid-structure Interaction Interface

The fluid-structure interaction is based on a time-domain partitioned solution process in which the nonlinear partial differential equation governing the fluid and the structure are solved independently and spatially coupled through the interface between the fluid and the structure. An interface module has been added to the fluid solver to communicate the parallelized flow solutions on the three-dimensional wetted surface to and from the serial structural solver. At each time step the fluid and the structural solvers are called one after the other until sufficient convergence on the displacements on the shared boundary surface are reached in an inner-iteration before advancing to the next time step. Full details of this algorithm are described in Refs. [19] and [20].

In the current study, in order to accelerate and ensure the convergence of the FSI the Aitken relaxation method[28] has been incorporated. The Aitken relaxation method is a fixed-point FSI-coupling method with dynamic relaxation. The fluid-structure coupling for partitioned domain can be summarized for the FSI-interface Γ as,

$$\widetilde{\boldsymbol{d}}_\Gamma^{n+1} = \boldsymbol{S}_\Gamma^{-1}\left(\boldsymbol{F}_\Gamma(\boldsymbol{d}_\Gamma^{n+1})\right), \tag{5}$$

where $\boldsymbol{F}_\Gamma$ denotes the fluid solver, $\boldsymbol{S}_\Gamma$ is the structural solver, $\boldsymbol{d}_\Gamma^{n+1}$ is the displacement of the interface Γ at the next time level $n+1$, and $\widetilde{\boldsymbol{d}}_\Gamma^{n+1}$ is the displacement output from the structural solver.

For weakly coupled systems $\widetilde{\boldsymbol{d}}_\Gamma^{n+1} \approx \boldsymbol{d}_\Gamma^{n+1}$ and the so-called explicit coupling can be used where the information between the fluid solver and the structural solver is communicated only once. If the structure is very light and flexible, the fluid forces will impact the structural deformations dominantly. Then the added mass effects become important and either monolithic solver or strongly coupled implicit scheme with sub-iterations is necessary[28]. In such an iterative coupling the Eq. (5) becomes

$$\widetilde{\boldsymbol{d}}_{\Gamma,i+1}^{n+1} = \boldsymbol{S}_\Gamma^{-1}\left(\boldsymbol{F}_\Gamma\left(\boldsymbol{d}_{\Gamma,i}^{n+1}\right)\right), \tag{6}$$

where now i is the iterator over the FSI-coupling.

In order to ensure and accelerate convergence of the iteration, a relaxation step is needed after each FSI-subiteration in Eq. (6),

$$\boldsymbol{d}_{\Gamma,i+1}^{n+1} = \omega_i \widetilde{\boldsymbol{d}}_{\Gamma,i+1}^{n+1} + (1-\omega_i)\boldsymbol{d}_{\Gamma,i}^{n+1}. \tag{7}$$

There are a number of methods to dynamically determine the relaxation factor ω_i:

- Prefixed: the relaxation factor should be sufficiently small to prevent the divergence of the FSI coupling, but large enough to reduce unnecessary FSI-iterations. It can be hard to find an optimum value.
- Aitken's relaxation[28]: By using secant like method for the unknown displacements, a recursive expression for the relaxation parameter can be estimated. This method has been implemented and will be explained below.
- Vector Extrapolation: This methods predicts the approximate solutions based on the first elements of a converging vector series, see Ref. [29]
- Jacobian-free Newton-Krylov Methods, Broyden methods, see Ref. [30] for descriptions and performance evaluations.

The Aitken's relaxation parameter for Eq. (7) is given by

$$\omega_{i+1} = -\omega_i \frac{\left(\boldsymbol{r}_{\Gamma,i+1}\right)^T \left(\boldsymbol{r}_{\Gamma,i+2} - \boldsymbol{r}_{\Gamma,i+1}\right)}{\left|\boldsymbol{r}_{\Gamma,i+2} - \boldsymbol{r}_{\Gamma,i+1}\right|^2} \tag{8}$$

where the residual is given as $\boldsymbol{r}_{\Gamma,i+1} = \tilde{\boldsymbol{d}}_{\Gamma,i+1} - \boldsymbol{d}_{\Gamma,i}$. The idea is to use the residuals from the previous two iterations to predict the solution using the secant method. In the vector extrapolation methods[29] larger number of residuals from the previous iterations are used, however Kütter and Wall[28, 29] showed that the Aitken method is simpler to implement and often provides faster convergence. The fluid and the structural solutions are considered to be synchronized for given tolerance ϵ if $\left|\boldsymbol{r}_{\Gamma,i+1}\right|_2 < \epsilon$ for $i \geq N_{\text{FSI}}$. N_{FSI} gives the number of FSI-subiterations. In the present study the convergence tolerance of $\epsilon = 1.0\times10^{-6}$ is used.

B. Dimensional Analysis and Non-dimensional Governing Equations

The relevant physical quantities are the density, ρ_f and the viscosity, μ, of the fluid; the reference velocity, U_{ref}, of the fluid flow; the half span, R, the mean chord, c_m, and the thickness, h_s, of the wing geometry; the structural density, ρ_s, the Young's modulus, E, and the Poisson's ratio, ν, of the wing structure; the flapping (plunging) amplitude, ϕ_a (h_a), the flapping frequency, ω the geometric angle of attack, α; and finally the resulting aerodynamic force, F. The wing kinematics are given by

$$\text{flapping: } \phi = \phi_a \sin(\omega t), \qquad \text{plunging: } h = h_a \cos(\omega t). \tag{9}$$

There are 13 variables and 3 dimensions leading to 10 non-dimensional parameters. With ρ_f, U_{ref}, and c_m as the basis variables the dimensional analysis leads to the non-dimensional parameters shown in Table 1.

If the reference velocity, U_{ref}, is chosen as the velocity scale, inverse of the motion frequency, $2\pi/\omega$, as the time scale, and the mean chord, c_m, as the length scale, the governing equations Eqs (1), (2), (3) and (4) and the motion kinematics Eq. (9) are non-dimensionalized as

$$\frac{\partial u_i^*}{\partial x_i^*} = 0, \tag{10}$$

$$\frac{k}{\pi}\frac{\partial u_i^*}{\partial t^*} + \frac{\partial u_j^* u_i^*}{\partial x_j^*} = -\frac{\partial p^*}{\partial x_i^*} + \frac{1}{Re}\frac{\partial}{\partial x_j^*}\left(\frac{\partial u_i^*}{\partial x_j^*}\right), \tag{11}$$

$$\rho^* h_s^* \left(\frac{k}{\pi}\right)^2 \frac{\partial^2 w_3^*}{\partial t^{*2}} + \Pi_1 \frac{\partial^4 w_3^*}{\partial x_1^{*4}} = f^*, \tag{12}$$

$$\rho^* h_s^* \left(\frac{k}{\pi}\right)^2 \frac{\partial^2 w_3^*}{\partial t^{*2}} + \Pi_1 \left(\frac{\partial^4 w_3^*}{\partial x_1^{*4}} + 2\frac{\partial^4 w_3^*}{\partial x_1^{*2}\partial x_2^{*2}} + \frac{\partial^4 w_3^*}{\partial x_2^{*4}}\right) = f^*, \tag{13}$$

$$\text{flapping: } \phi = \frac{St}{k\,AR}\sin(2\pi t^*), \qquad \text{plunging: } \frac{h}{c_m} = St\frac{\pi}{k}\cos(2\pi t^*). \tag{14}$$

Table 1. Non-dimensional parameters for the FSI system with their physical relevance.

Non-dimensional parameter	Definition	Description
Reynolds number	$Re = \frac{\rho_f U_{\text{ref}} c_m}{\mu}$	Ratio between the inertial and the viscous forces in the fluids
Aspect ratio	$AR = \frac{4R}{c_m}$	Wing span normalized with the chord
Normalized thickness	$h_s^* = h_s/c_m$	Thickness normalized with the chord
Density ratio	$\rho^* = \rho_s/\rho_f$	Ratio between the structural density and the fluid density
Poisson's ratio	ν	Ratio between the transverse and the axial strain
Effective stiffness	$\Pi_1{}^{**} = \frac{E h_S^{*3}}{12(1-\nu^2)\rho_f U_{\text{ref}}^2}$	Ratio between the elastic bending forces and the aerodynamic force
Reduced frequency	$k = \frac{\omega c_m}{2U_{\text{ref}}}$	Measure of unsteadiness by comparing the spatial wavelength of the flow disturbance with the chord
Strouhal number (flapping)	$St = k(AR)\phi_a$	Ratio between the flapping speed and the reference velocity
Strouhal number (plunging)	$St = \frac{k}{\pi}\frac{h_a}{c_m}$	
Angle of attack	α	Curvature of the streamlines leading to pressure changes on the wing surface
Force coefficient	$C_F = \frac{F}{1/2\rho_f U_{\text{ref}}^2 (2c_m^2 AR)}$	Aerodynamic force normalized with the dynamic pressure and the wing surface area

III. Results and Discussions

A. Isotropic Elliptic Flapping Wing in Still Air at $Re = 1.5\times10^3$

1. Case Setup

The wing is a flat plate wing with Zimmerman planform[20], see Figure 1, flapping in still air at $Re = 1.5\times10^3$. The motion is excited at the rigid triangle at the leading edge at the wing root with a sinusoidal motion, see Eq. (15), as

$$\phi(t) = \phi_a \sin(\omega t), \tag{15}$$

where $\phi(t)$ is the instantaneous flapping angle, ϕ_a the flapping amplitude, and ω the motion angular frequency. The flapping axis is parallel to the wing root, see Figure 1. The relevant parameters for the baseline case reported in Ref. [20] are repeated in Table 2.

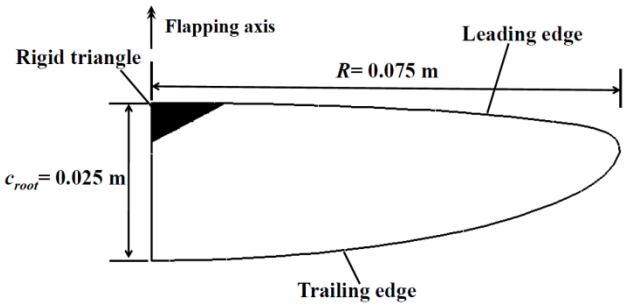

Figure 1. Geometry of the Zimmerman planform used in the current study.

** For the Euler-Bernoulli beam model the effective stiffness is defined as $\Pi_1 = E\bar{h}_s^3/\left(12\rho_f U_{\text{ref}}^2\right)$.

Table 2. Dimensional and non-dimensional parameters for the baseline case.

Parameter		Value	Non-dimensional Parameter	Value
R	[m]	7.5×10^{-2}	Re	1.5×10^{3}
c_m	[m]	1.96×10^{-2}	St	0.25
h_s	[m]	4.0×10^{-4}	k	0.56
U_{ref}	[m/s]	1.10 (tip speed)	AR	7.65
ρ_f	[kg/m^3]	1.23	h_s^*	2.0×10^{-2}
E	[kg/ms^2]	70×10^{9}	Π_1	3.8×10^{4}
ν	[1]	0.3	ρ^*	2.2×10^{3}
ρ_s	[kg/m^3]	2.7×10^{3}		
ϕ_a	[deg]	21		
$\omega/(2\pi)$	[1/s]	10		

The computational grid to solve the Navier-Stokes equations Eq. (1) and (2) consists of mixed brick and tetrahedral cells around the Zimmerman wing, see Figure 2a). The analyses of the spatial and the temporal sensitivities can be found in the Appendix A. A triangular region near the root at the leading edge undergoes prescribed motion and is constrained in all degrees of freedom in the structural solver, since the flapping mechanism in the experiment[20] is actuated at this region on the wing. A total of 767 shell elements (437 nodes) are used in the finite element discretization in co-rotational framework. The CFD (computational fluid dynamics) and CSD (computational structural dynamics) grid configurations are shown in Figure 2.

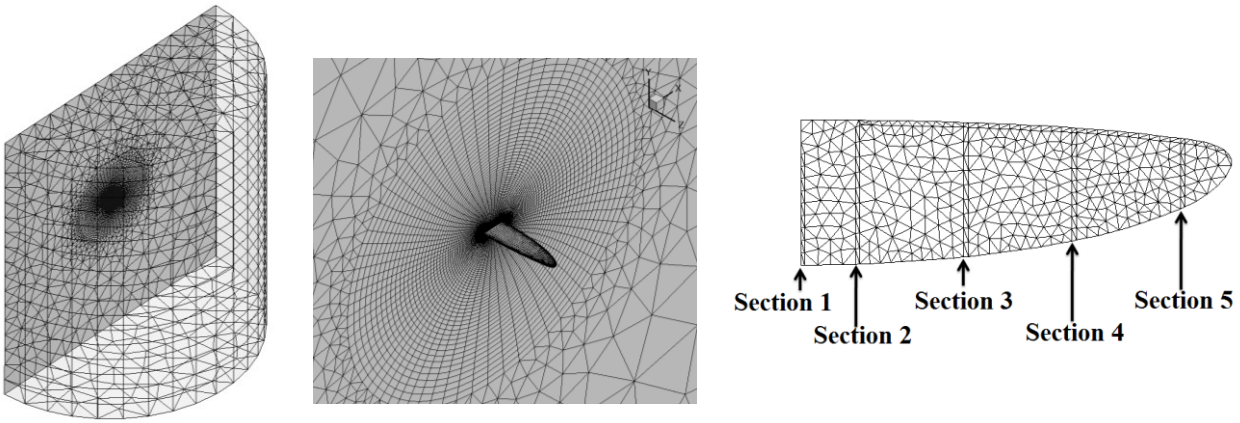

(a) Computational grid for the CFD simulations (b) Computational grid for the CSD simulations

Figure 2. Computational grids for the isotropic Zimmerman wing in flap motion.

2. Design of Experiments and Surrogate Models

The baseline case[20] and the previous studies[10, 21] showed that the flexibility-induced pitching angle promotes the thrust generation and the increase of wing velocities due to large bending motion enhance aerodynamic force by increasing pressure differences. To assess the applicability of this observation for different wing properties, the effective stiffness Π_1 and the density ratio ρ^* have been chosen as the design variables to construct surrogate models to qualitatively explore their implications on the resulting thrust generation. The range for these variables in the design space is chosen to cover wide range of applications as shown in Table 3. To effectively assess the order of magnitude of the design variables a logarithmic scaled design space will be populated.

Table 3. Minimum and maximum values of the effective stiffness and the density ratio.

Parameter	Minimum	Baseline[20]	Maximum
Π_1	1.0×10^{2} (HDPE, polyethylene in air)	3.8×10^{4}	1.0×10^{5} (steel, aluminum in air)
ρ^*	1.0×10^{1} (water to steel, aluminum)	2.2×10^{3}	1.0×10^{4} (air to steel, aluminum)

The objective functions are the time-averaged thrust, the bending angle, the twist, and time-averaged number of FSI-subiterations, N_{FSI}, where the instantaneous coefficients are defined as

$$C_T = \frac{T}{\frac{1}{2}\rho_f U_{\mathrm{ref}}^2 \left(2c_m^2 AR\right)}, \tag{16}$$

with AR the aspect ratio of the wing and T thrust, so that for the resulting force, F_i, we have $T = -F_2$. For simplicity thrust will be referred as the time averaged thrust coefficient from now on. The bending angle is defined as the maximum tip displacement angle relative to the instantaneous prescribed flap angle,

$$\text{bending angle} = \max\{\tan^{-1}(w_3/R) - \phi\}. \tag{17}$$

with w_3 the wing tip displacement in the vertical direction. Similarly, the twist angle is defined as the maximum projection angle along the chord at the section 3, see Figure 2b),

$$\text{twist} = \max\{\cos^{-1}(\boldsymbol{c_3} \cdot \boldsymbol{e})\}, \tag{18}$$

where $\boldsymbol{c}_3$ is the unit vector in the direction from the leading edge to the trailing edge at the section 3 of the wing and $\boldsymbol{e}$ is the unit vector in the thrust direction. So the twist angle gives the degree of the thrust favorable projectional area of the wing due to deformation.

The design of experiments use a face centered cubic design (FCCD) and then the remainder of the design space is appropriately filled. In total 10 training points are selected. A tabulation of the training points are found in Table 5 in the Appendix B. The design space with logarithmic bias towards the softer (Π_1) and lighter (ρ^*) structures are shown in Figure 3. The region where $\log_{10}\rho^* > \log_{10}\Pi_1 + 2$ is out of the scope of the current study as this region showed largely unstable behavior of the wing motion because the imposed frequency of 10 Hz is close to the natural frequencies, see Figure 16and Table 6 in the Appendix 0 for the natural frequencies and modes for each cases.

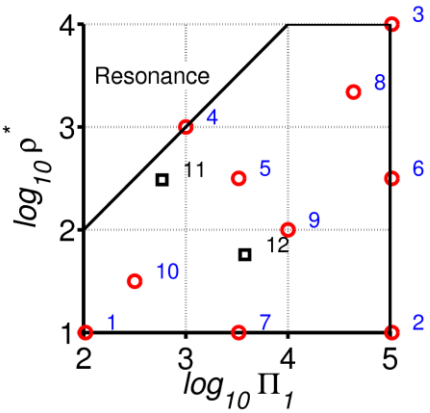

Figure 3. Design of experiment in logarithmic scale for the design variables Π_1 and ρ^*. All vertices, center of edges, and the center of the domain are occupied with a training point (○) using the FCCD and the resting three points are properly filled. Two testing points (□) are placed in the regions of interest.

Different weighting strategies are employed to minimize the risk of generating surrogates that fit the training data well but perform less in other regions. The weighted average surrogates (WAS) use constant weights, meaning

that a certain surrogate will have the same importance throughout the design space. The Polynomial Response Surface, Kriging, and Support Vector Regression are used for the individual surrogates, see Table 7 in the Appendix D, after which each surrogates are weighted in correlation to the RMS PRESS values, defined as

$$\text{RMS PRESS} = \sqrt{\frac{1}{N_s}\sum_{i=1}^{N_s}\left(y_i - \hat{y}_i^{(-i)}\right)}, \tag{19}$$

where $\hat{y}_i^{(-i)}$ is the prediction at $x^{(i)}$ using a surrogate model constructed with all training point except $x^{(i)}$, and N_s is the number of training points. Table 4 shows the RMS PRESS values as predicted by the individual surrogate models for the thrust, twist, bending, and time averaged number of FSI-subiterations. The cells with bold fonts indicate the lowest RMS PRESS values and the surrogates that are weighted in the WAS. The error measured at the independent testing points defined as the relative difference between the constructed WAS and the actual values from the simulations with respect to the range of the objective functions show, see Table 8 in the Appendix E, that for the case 11 where the high gradients in the surrogates are located has larger error than for the more stiffer case 12.

Table 4. PRESS values as predicted by the individual surrogate models for the thrust, bending angle, twist, and time averaged number of FSI-subiterations. Surrogate models indicated by the bold fonts are used for the WAS construction.

	KRG	**PRS**	**SVR1**	**SVR2**	**SVR3**	**SVR4**	**SVR5**	**SVR6**
$< C_T >$	$\mathbf{3.7\times10^{-1}}$	5.6×10^{-1}	5.8×10^{-1}	3.9×10^{-1}	$\mathbf{3.3\times10^{-1}}$	$\mathbf{3.2\times10^{-1}}$	5.3×10^{-1}	3.9×10^{-1}
twist	4.2×10^{-1}	6.1×10^{-1}	6.5×10^{-1}	4.5×10^{-1}	$\mathbf{3.7\times10^{-1}}$	$\mathbf{3.5\times10^{-1}}$	6.1×10^{-1}	4.8×10^{-1}
bending	3.9×10^{-1}	5.3×10^{-1}	5.6×10^{-1}	3.7×10^{-1}	$\mathbf{3.3\times10^{-1}}$	$\mathbf{3.1\times10^{-1}}$	5.2×10^{-1}	3.7×10^{-1}
$< N_{\text{FSI}} >$	3.9×10^{-1}	$\mathbf{3.0\times10^{-1}}$	4.0×10^{-1}	4.7×10^{-1}	$\mathbf{2.6\times10^{-1}}$	$\mathbf{2.9\times10^{-1}}$	$\mathbf{3.0\times10^{-1}}$	$\mathbf{3.0\times10^{-1}}$

The resulting surrogates are shown in Figure 4 for the thrust, twist, bending angle, and time averaged number of FSI-subiterations. The thrust, twist, and bending have maximum at the case 4 ($\rho^* = 1.0\times10^3$ and $\Pi_1 = 1.0\times10^3$) and these three objective functions have qualitatively similar trend in the design space. It is not only the effective stiffness (Π_1), or the density ratio (ρ^*), but the balance between these two parameters that determine the resulting deformation and the thrust generation. The number of FSI-subiterations increases for lower ρ^* and smaller Π_1. This is consistent with the previous findings[28, 29] that light material (low ρ^*) and softer material (small Π_1) leads to tighter FSI-coupling, hence more FSI-subiterations are required to synchronize the partitioned coupling. Scaling parameters related to the thrust and the degree of FSI-coupling will be discussed further in Section III.C and III.D.

As the sinusoidal rigid-body motion is imposed at the triangular rigid part near the wing root (see Figure 1), the wing inertia and the resulting aerodynamic load is balanced out by the elastic force. Since the wing is made of isotropic material the structure will response in both spanwise bending as well as chordwise twisting. Two thrust enhancement mechanisms due to flexibility were found previously: i) the twist redistributes the resulting aerodynamic force in thrust favorable direction[10, 33], ii) the spanwise bending enhances the thrust if the phase angle is acute[10]. The interplay between the resulting thrust, and the wing twist and bending will be highlighted for the *Maximum Thrust* (case 4) and the *Medium Thrust* (case 1) cases.

Figure 5 shows the time history of thrust coefficient as function of time for the *Maximum Thrust*, *Medium Thrust,* and *Minimum Thrust* (rigid) cases. The time histories of C_T of all other cases lie between the *Maximum Thrust* and the *Minimum Thrust* cases, which indicate that instantaneous thrust is always positive for all cases. Furthermore, one thrust peak per stroke is seen between the beginning of the stroke and the middle of stroke.

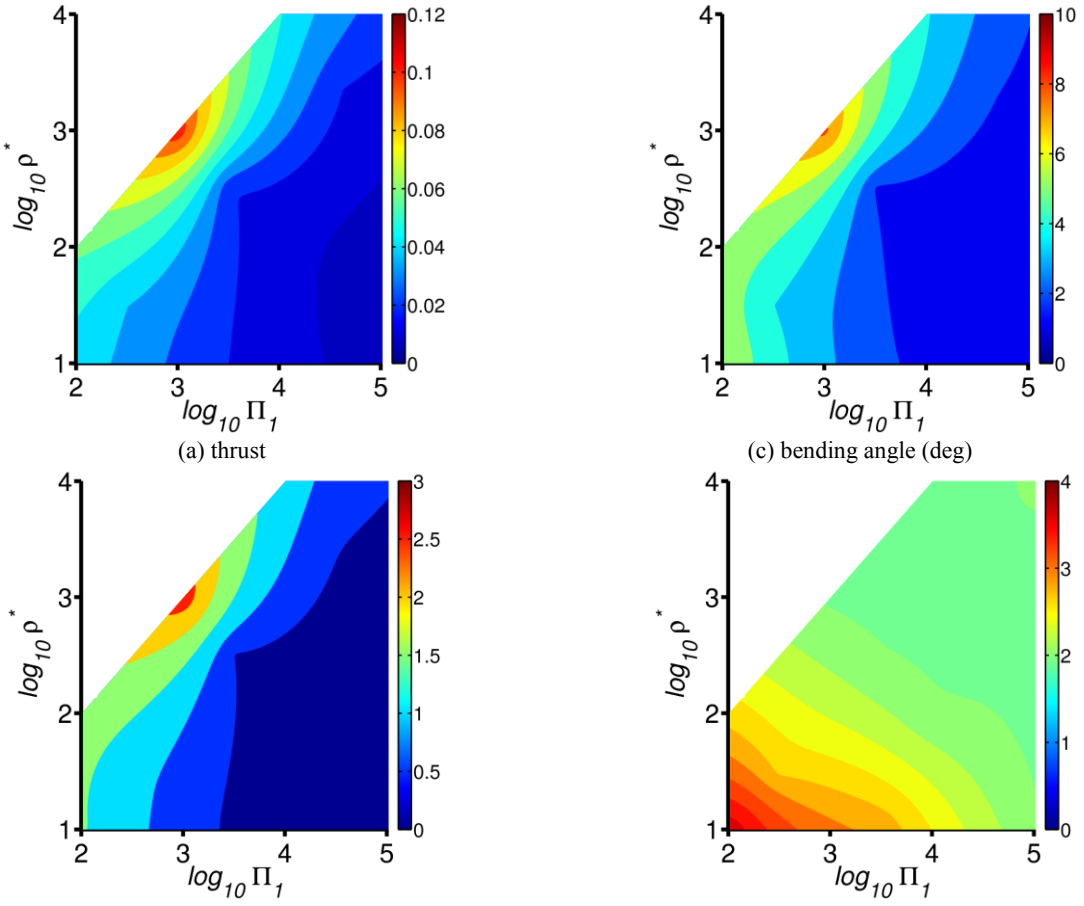

Figure 4. Surrogate models for (a) thrust, (b) twist, (c), bending angle, and (d) time averaged number of the FSI-subiterations for a flapping isotropic Zimmerman wing at $Re = 1.5\times10^3$ and $k = 0.56$.

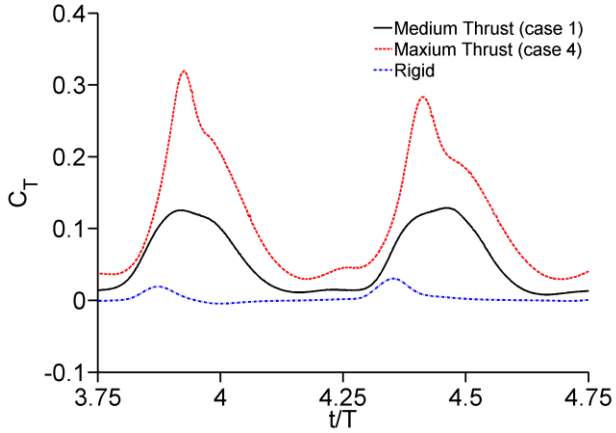

Figure 5. Time history of thrust coefficient as function of time for a flapping isotropic Zimmerman wing at $Re = 1.5\times10^3$ and $k = 0.56$ for the *Medium Thrust* (red, dot), *Maximum Thrust* (black, solid), and *Minimum Thrust* (blue, dashed) cases.

Figure 6 shows the phase diagrams of the bending angle at the wing tip and the twist angles at five different spanwise sections, i.e. section 1: 0% (root), section 2: 12.5%, section 3: 37.5% (max), section 4: 62.5%, and section 5: 87.5% (near tip), see also Figure 2b), as functions of the flap angle for the *Maximum Thrust* and the *Medium Thrust* cases. As indicated by the surrogate model results, both the tip bending angle and the twist are larger for the *Maximum Thrust* case than the *Medium Thrust* case. Furthermore, the phase angle[49], which indicates the degree of

how much the deformed wing motion is in phase with the prescribed rigid-body motion at the root, shows that again the *Maximum Thrust* has smaller phase angle, hence less phase lag, than the *Medium Thrust*. Both observations are consistent with the obtained thrust computation and further studies are planned to quantify the individual contributions from the twist and bending.

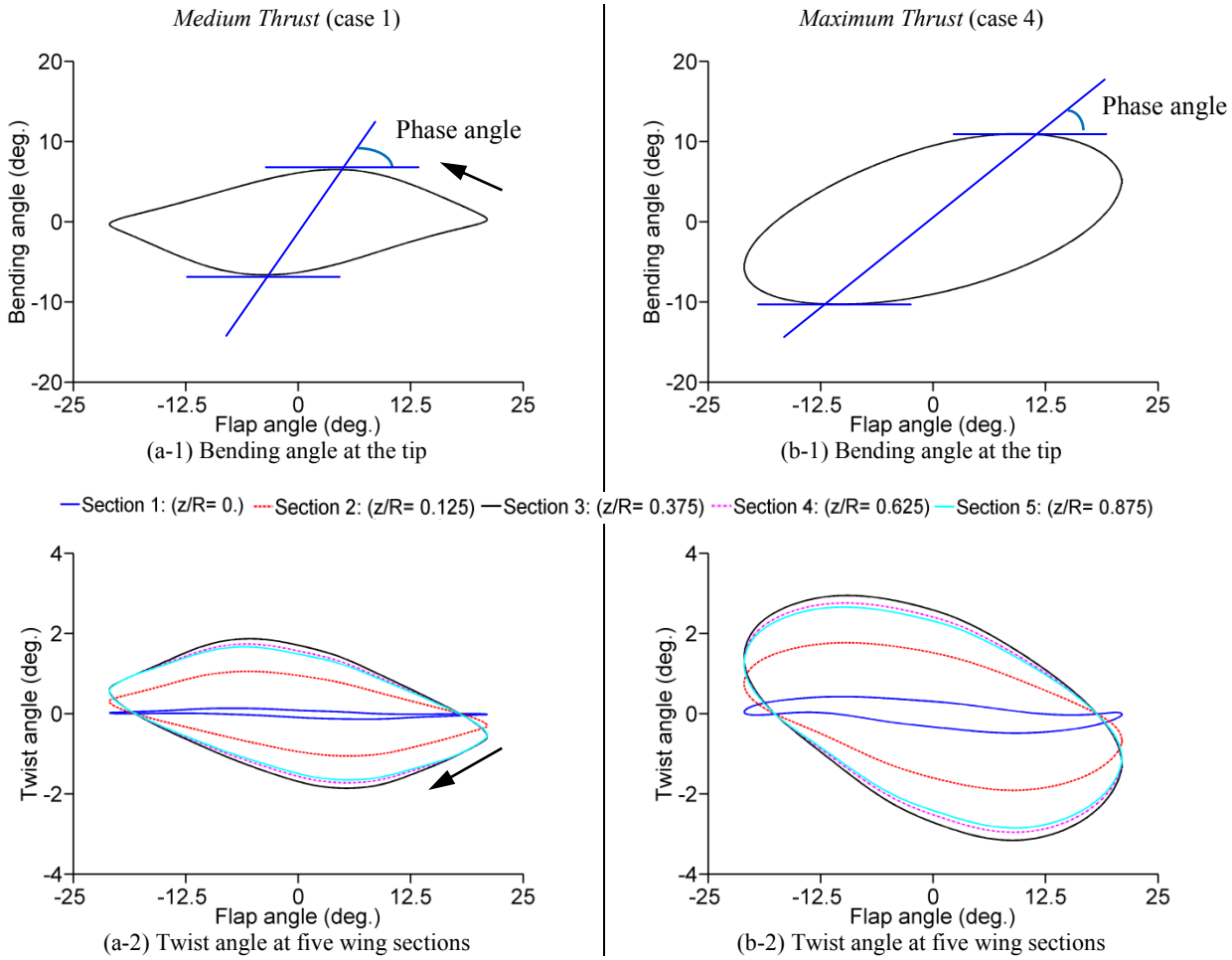

Figure 6. Tip bending angles and twist angles at five spanwise sections for a flapping isotropic Zimmerman wing at Re = 1.5×10^3 and k = 0.56 for the (a) *Medium Thrust* (case 1) and (b) *Maximum Thrust* (case 4) cases. Note that the phase loops go in counter clockwise direction for the bending angles (a-1) and (b-1), and in clockwise direction for the twisting angles (a-2) and (b-2).

Figure 6 shows that, for both cases, the shapes of the phase diagrams are qualitatively similar to each other, with larger maximum twist and bending angles for the *Maximum Thrust* case. The relation between the twist and the bending angles is summarized in Figure 7 showing that there is almost linear correspondence between the twist and the bending for both cases. Figure 8 shows the phase diagrams of the instantaneous thrust as function of the bending and twist angles (section 3) for the *Maximum Thrust* and the *Medium Thrust* cases. For both cases the thrust is at maximum slightly before the wing reaches its maximum bending angle. The maximum twist gives, on the other hand, the maximum thrust for both cases. Therefore, the wing deformation (i.e. large bending and twist of the wing) promotes thrust generation for the cases considered in current study.

Figure 9 illustrates the normalized spanwise vorticity contours at the mid span for the *Maximum Thrust* and the *Medium Thrust* cases at t/T= 3.75, 3.95 (near maximum C_T), 4.1, and 4.25, together with the time histories of the twist angles at section 3, see Figure 6 a-2) and b-2). The higher thrust generation for the *Maximum Thrust* case can be correlated to the flow structures as follows:

- t/T= 3.75: Top of the stroke. Both the leading edge vortex (LEV) and the trailing edge vortex (TEV) are stronger due to larger bending, hence higher wing velocities compared to the *Medium Thrust*.

- t/T= 3.95: As the wing flaps down the wing velocity increased and LEV and the TEV have already formed. At the trailing edge two counter-rotating vortices interact with each other and result in a stronger induced velocity as indicated by the white arrow. At this time instant the twist and the thrust are also close to maximum.
- t/T= 4.10: As the wing decelerates the twist reduces to zero, the flow field is almost symmetric, and the thrust drops to minimum
- t/T = 4.25: Bottom of the stroke. The *Maximum Thrust* case shows lower wing position due to larger spanwise bending deformation. This will eventually lead to stronger vortices and higher thrust. Note also that the TEV is weaker than the TEV shown in Figure 9a) consistent with smaller peak between t/T = 4.25 and 4.5 compared to the peak near t/T = 4.

Again, Figure 9 suggests that the time instant of the maximum thrust corresponds to the maximum twist.

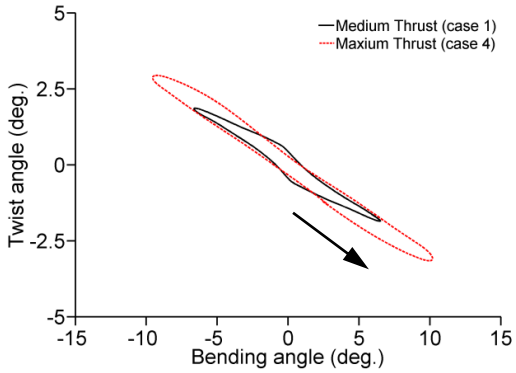

Figure 7. Twist (section 3) as function of the bending angle for a flapping isotropic Zimmerman wing at Re = 1.5×10^3 and k = 0.56 for the *Medium Thrust* (black, solid) and the *Maximum Thrust* (red, dashed) cases.

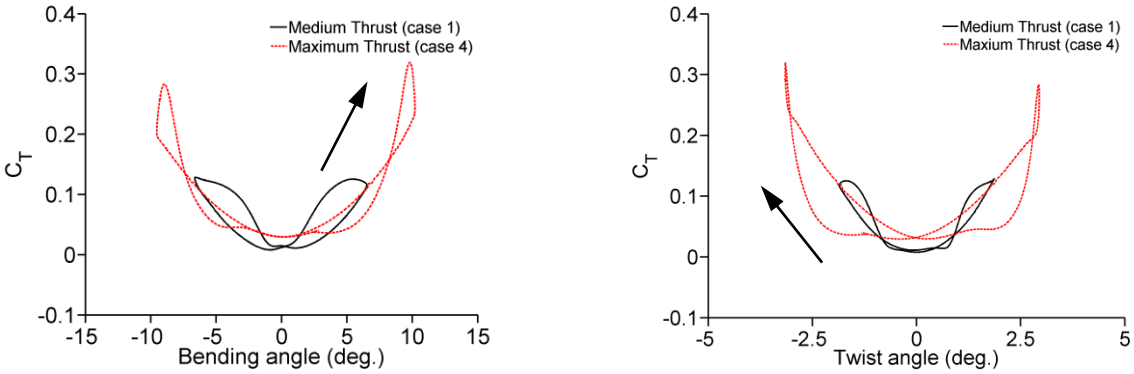

(a) Thrust vs bending anlge (b) Thrust vs twist anlge

Figure 8. Phase loops of the thrust as function of bending (a) and twist (b) angles for a flapping isotropic Zimmerman wing at Re = 1.5×10^3 and k = 0.56 for the *Medium Thrust*(black, sold) and the *Maximum Thrust* (red, dashed) cases.

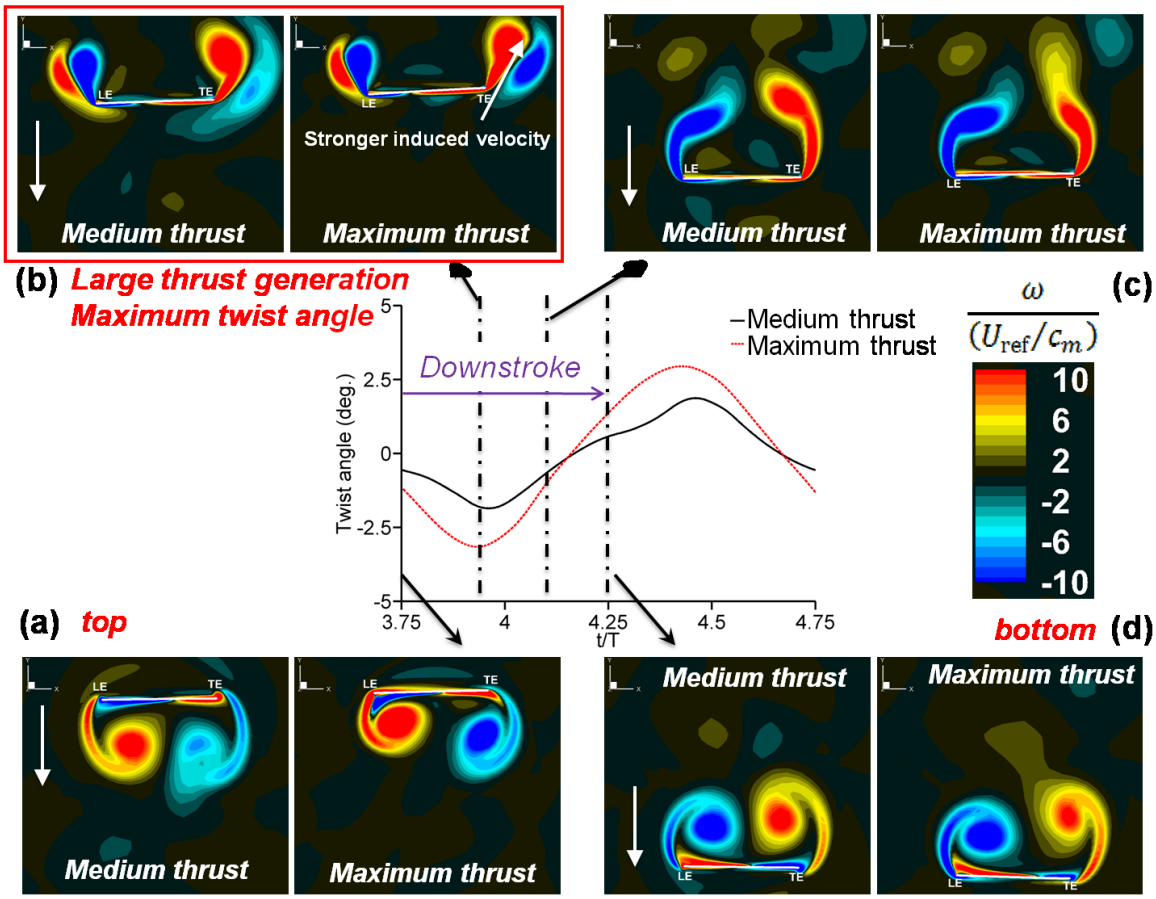

Figure 9. Normalized spanwise vorticity contours at the mid-span at (a) t/T = 3.75 (top), (b) t/T = 3.95, (c) t/T = 4.1, and (d) t/T = 4.25 (bottom) for the *Medium Thrust* and the *Maximum Thrust* cases. Note that LE and TE indicate leading edge and trailing edge.

B. Chordwise Flexible Airfoil in Forward Flight at $Re = 9.0\times10^3$ in Water

The isotropic flapping Zimmerman wing suggests that the thrust generation is directly related to the degree of chordwise deformation. To explore the flexibility induced thrust enhancement further, the thrust of a purely plunging chordwise flexible airfoil[7, 10] are computed for different thickness ratios (h_s^* = 4.23×10^{-3}, 1.41×10^{-3}, and 0.56×10^{-3}) and motion frequencies. The airfoil consists of a rigid teardrop leading edge and an elastic plate that plunges sinusoidally in freestream. Detailed case setup can be found in Refs. [7] and [10]. An Euler-Bernoulli beam solver is used to solve the Eq. (12) for the deformation of the elastic flat plate. The Reynolds number Re = 9.0×10^3, the plunge amplitude ratio h_a/c_m = 0.194, and the density ratio ρ^* = 7.8 are held constant in all cases.

Figure 10 shows the time-averaged thrust coefficient for a range of motion frequencies so that the corresponding Strouhal numbers and reduced frequencies vary from St = 0.085 to 0.4 and k = 1.2 to 6.5 from the current numerical computation and the experimental measurements[7]. The thrust coefficients correlate very well except for the inflexible case (h_s^* = 4.23×10^{-3}) at higher frequencies, $Sr = 2\,St > 0.7$. The reason is not yet determined and will be reported in the future. The thrust increases with increasing motion frequency (i.e. Strouhal number).

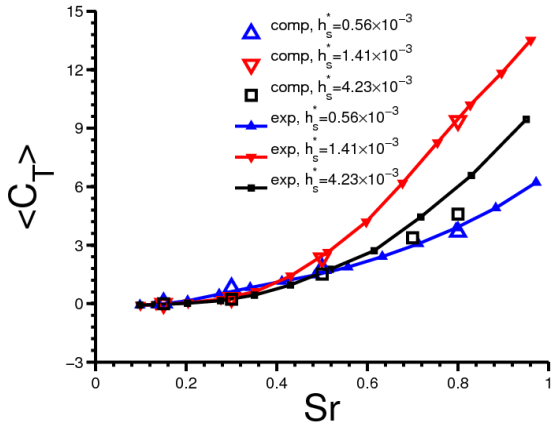

Figure 10. Time averaged thrust coefficient for a plunging chordwise flexible airfoil at $Re = 9.0\times10^3$ and $\rho^* = 7.8$ for different flexibility and motion frequencies. The experimental data were extracted from Heathcote and Gursul [7]. The Strouhal number definition in this follows that of Heathcote and Gursul [7], i.e. $Sr = \omega h_a/\pi U_{\text{ref}} = 2\,St = 2(k/\pi)(h_a/c)$.

The thrust for an inflexible airfoil (h_s^* = 4.23×10^{-3}) can be enhanced by increasing the Strouhal number, which influences the LEV generation and wing-wake interaction, and hence thrust generation. Introducing the flexibility by reducing the flat plate thickness, the thrust increases for sufficiently large Strouhal number. The thinnest airfoil (h_s^* = 0.56×10^{-3}) has the highest thrust at Sr = 0.3, however as the thrust deteriorates for larger Strouhal numbers. Eventually, the fluid dynamics time scale and structural responses become limiting factors. The results shown in Figure 10 suggest that the Strouhal number or the thickness ratios are not the correct non-dimensional parameters to scale the thrust for flexible flapping wings.

C. Scaling Parameter for the Degree of FSI-coupling

Before discussing the thrust, the degree of FSI-coupling measured by the time averaged number of the FSI-subiterations is investigated. Consider both structural dynamics equations, Eqs. (12) and (13), which have the same form:

$$\Pi_0 \cdot \text{Inertia} + \Pi_1 \cdot \text{Elasticity} = \text{Force}_{\text{fluid}}, \tag{20}$$

where $\Pi_0 = \rho^* h_s^* \left(\frac{k}{\pi}\right)^2$ is the effective inertia term. The non-linearity and also the coupling to the fluid dynamics are introduced in the RHS of Eq. (18). The deforming wing changes the momentum of the fluid and at the same time the flow field will exert pressure and viscous forces on the surface of the wing that in turn will affect the displacement field. The fluid force term in the RHS of Eq. (20) is simplified as follows. For a harmonically plunging thin flat plate without pitching motion the added mass term[50] becomes, see also Appendix G,

$$c_l = \frac{\pi c_m}{2}\frac{\ddot{h}}{U_\infty^2} \sim \frac{f^2 h_a c_m}{U_\infty^2} \sim St \cdot k, \tag{21}$$

which will dominate over the circulatory term if the reduced frequency is sufficiently large. In the current approximation only the added mass term is used to estimate the aerodynamic force. Then, Eq. (20) can be approximated as,

$$\Pi_0 \cdot \text{Inertia} + \Pi_1 \cdot \text{Elasticity} = St \cdot k \cdot O(1). \tag{22}$$

Since the RHS of Eq. (22) gives the coupling to the fluid dynamics, divide both sides of Eq. (22) by $St \cdot k$, which yields,

$$\frac{\Pi_0}{St \cdot k} \cdot \text{Inertia} + \frac{\Pi_1}{St \cdot k} \cdot \text{Elasticity} = O(1). \tag{23}$$

If either $\Pi_0/St \cdot k$, or $\Pi_1/St \cdot k$ (or both) are small compared to $O(1)$, then the coupling algorithm explained in the Section II.A.3 with the relaxations for the wing displacements, hence for the resulting fluid dynamics force field on the structure, needs more FSI-subiterations to converge to the synchronized time accurate solution. To represent this idea the scaling parameter for the degree of FSI-coupling is proposed as,

$$\gamma_{\text{FSI}} = \frac{St \cdot k}{\Pi_0} \cdot \frac{St \cdot k}{\Pi_1}, \tag{24}$$

which is called the *FSI shape factor*. γ_{FSI} is consistent with the surrogate model result for $< N_{\text{FSI}} >$ in Figure 4. For the hovering Zimmerman wing case St and k are constant and Π_0 is represented by ρ^*. Figure 11 shows $< N_{\text{FSI}} >$ for both isotropic Zimmerman wing cases as well as the chordwise flexible airfoil cases plotted against γ_{FSI} in logarithmic scales. The number of FSI-subiterations depends monotonically on the FSI shape factor. Around $\gamma_{\text{FSI}} = 10^{-3}$ the time-averaged number of FSI-subiterations starts to increase, indicating fluid-structure system is more tightly coupled. For the FSI shape factor less than 10^{-3} the system can be regarded as loosely coupled and small number of communication between the fluid and structural solver is needed to synchronize the coupled solution. This scaling analysis shows that not only the density ratio or bending rigidity need to be considered to estimate the degree of the FSI-coupling, but also the reduced frequency, the thickness ratios, and the Strouhal number for a flapping flexible wing.

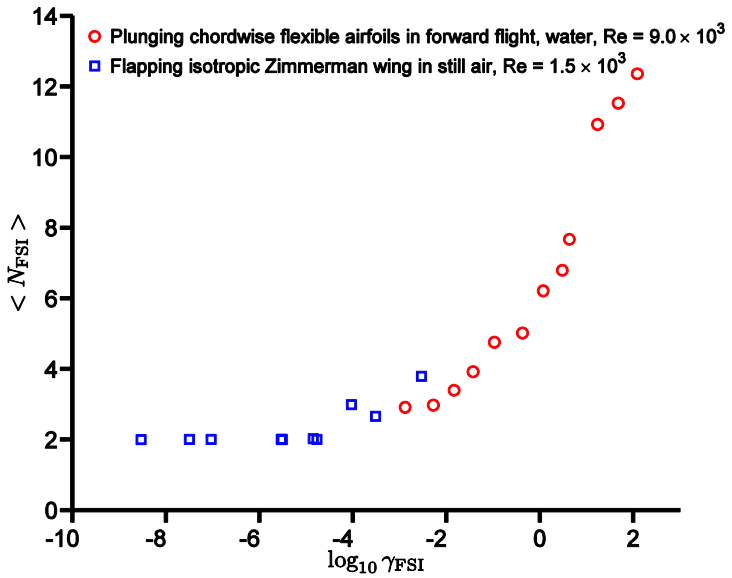

Figure 11. Time averaged number of FSI-subiterations as function of the FSI shape factor for the flapping isotropic Zimmerman wing and the purely plunging chordwise flexible airfoil cases.

D. Scaling Parameter for the Thrust

The surrogate model results in Figure 4 suggest that not only the effective stiffness plays a role in the thrust generation, but also the density ratio. The ratio between the density ratio and the effective stiffness has dominant role in the qualitative trend in thrust, which will be discussed in this section as $\Pi_0/\Pi_1 \sim \rho^*/\Pi_1$. The current study and previous works[10, 33] have shown that one of the mechanisms to enhance thrust is to enlarge the thrust promoting projected area by deformations: deformations lead to passive pitching motion of the flexible wings and the resulting aerodynamic force on the deformed wing is distributed in the thrust favorable direction[10]. To capture the essence of the scaling involved in the thrust enhancement due to flexibility, first, dimensional arguments will be used establish scaling in the limiting situations to predict qualitative trends. This will be followed by a correction term for the natural frequencies for the wing which follows from the analysis of the Eq. (12).

Eq. (22) contains three non-dimensional parameters. To scale the thrust enhancement due to elastic deformation, dividing Eq. (22) by Π_1 yields

$$\frac{\Pi_0}{\Pi_1} \cdot \text{Inertia} + 1 \cdot \text{Elasticity} = \frac{St \cdot k}{\Pi_1}, \tag{25}$$

where the elasticity term is of the order of unity. The other two terms Π_0/Π_1 and $(St \cdot k)/\Pi_1$ represent the importance of the inertia and the aerodynamic force with respect to the elasticity term. The ratio between the effective inertia (Π_0) and the effective stiffness (Π_1) can be related to a parameter introduced as the elastoinertial number, $\mathcal{N}_{ei} = \rho_f h_s h_a f^2 c_m^3/(E h_s^3)$, in Ref. [33] as it will be shown later: Π_0/Π_1 gives the balance between the inertia force and the elastic force under the application of coupled force by the fluid. Two parameters can be adjusted to obtain deformations that increase the thrust favorable projection area: larger force via $St \cdot k/\Pi_1$, or relatively lower stiffness compared to the inertia via Π_0/Π_1. Based on this argument, the scaling parameter for the thrust is proposed as the *thrust shape factor*:

$$\gamma = \frac{\Pi_0}{\Pi_1} \cdot \frac{St \cdot k}{\Pi_1}. \tag{26}$$

Figure 12 shows the time averaged thrust coefficient for the flapping isotropic Zimmerman wing computations as defined in Figure 3 and Table 5 as function of γ in logarithmic scales. Furthermore, numerical results from the purely plunging chordwise flexible airfoil cases in forward flight in water, see Section III.B, are added. The Zimmerman wing cases are parametrized by (Π_1, ρ^*) and the chordwise flexible airfoil cases by (f, h_s^*). For both cases the time-averaged thrust coefficients, see Table 9 in the Appendix F for the tabulated values, normalized by Π_1 show almost a linear dependency on γ in logarithmic scale.

.

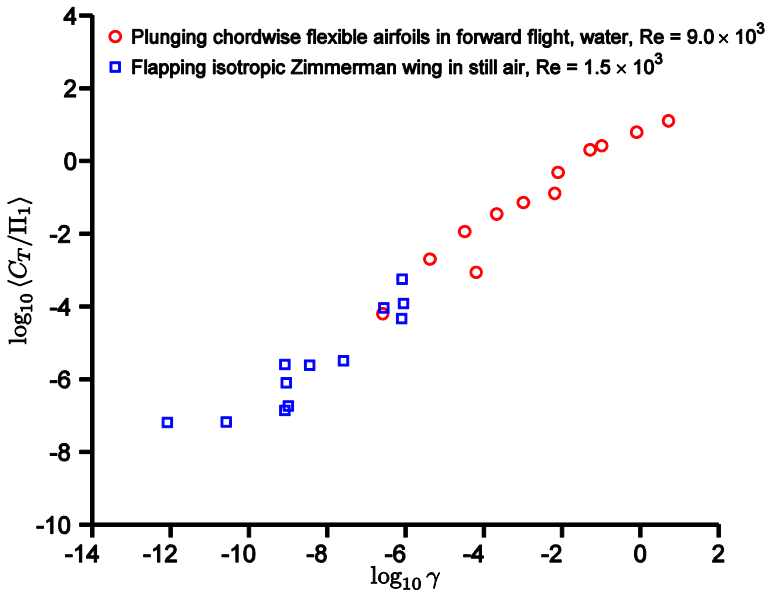

Figure 12. Normalized time averaged thrust coefficient as function of the thrust shape factor (dimensional argument) for the flapping isotropic Zimmerman wings in still air at Re = 1.5×10^3 and the purely plunging chordwise flexible airfoils in forward flight in water at Re = 9.0×10^3.

Different physical interpretation can be given to the Π_1/Π_0 ratio. Consider again Eq. (12) with the effective inertia as the coefficient for the inertia term,

$$\Pi_0 \frac{\partial^2 w_3^*}{\partial t^{*2}} + \Pi_1 \frac{\partial^4 w_3^*}{\partial x_1^{*4}} = f^*. \tag{12}$$

Eq. (12) is a beam equation where the square of the natural frequency of the system, ω_n, is given by a multiple of Π_1/Π_0, i.e.,

$$\omega_n^2 = \frac{k_n^4}{1^4}\frac{\Pi_1}{\Pi_0} = \left(\frac{2\pi f_n}{f}\right)^2, \tag{27}$$

where $k_n \approx (n + 1/2)\pi$ is a constant and f_n the natural frequency of the wing modeled as a beam. Hence Π_1/Π_0 is also proportional to the square of the ratio between the natural frequency of the wing and the excitation frequency. Comparing the thrust shape factor, γ, with the maximum tip deformation that follows from the analytic solution of Eq. (12) under the assumption of fluid forces contributed only by the added mass effects[50], see Appendix G for the solution, shows that γ needs to be corrected for the natural frequencies of the wing, f_n to account for the multiple time scales involved in the system: natural structural time scale $1/f_n$ and the motion time scale $1/f$ as follows:

$$\gamma_{\text{thrust}} = \frac{St \cdot k}{\Pi_0 \left\{\left(\frac{f_n}{f}\right)^2 - 1\right\}}, \tag{28}$$

which motivates to plot the normalized thrust against γ_{thrust} yielding Figure 13. Note that the inertial force term arising from the plunging boundary condition has been neglected because for the plunging chordwise flexible airfoils $\rho^* h_s^* \ll 1$ and for the flapping isotropic Zimmerman wing the motion type is different: A further study is planned to investigate the inertial term for the flapping motion.

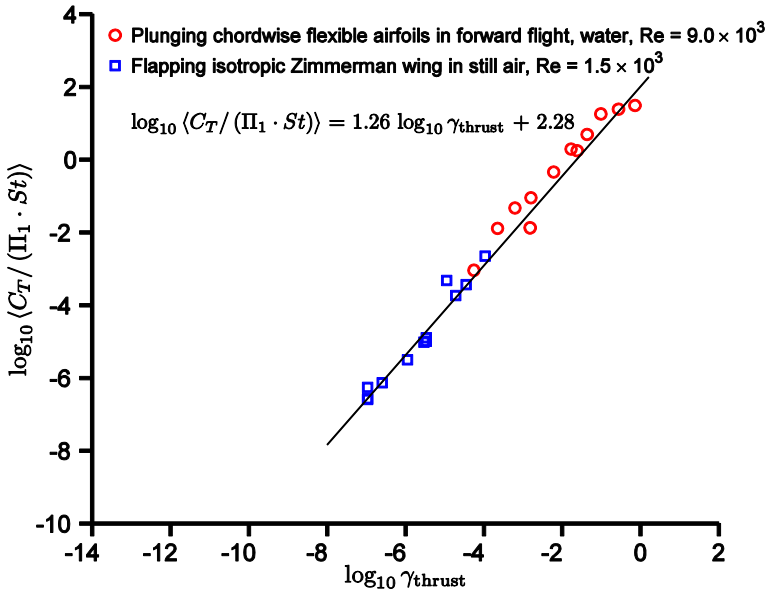

Figure 13. Normalized time averaged thrust coefficient as function of the corrected thrust shape factor (physical argument) for the flapping isotropic Zimmerman wing in still air at Re = 1.5×10^3 and the purely plunging chordwise flexible airfoil cases in water in freestream at Re = 9.0×10^3. The coefficient of determination for the linear fit in least square sense is 0.96.

Compared to the scaling shown in Figure 12 γ_{thrust} scales the time averaged thrust almost linearly in the logarithmic scale with less scatter than γ. The thrust shape factor, γ_{thrust} is also an extended scaling parameter of the elastoinertial number[33] defined by Thiria and Godoy-Diana[33]. It can be shown that under the assumptions of the excitation frequency much smaller than the natural frequency of the wing γ_{thrust} can be approximated by $\mathcal{N}_{ei}$ as follows. Assume that $f_n \gg f$, then γ_{thrust} defined in Eq. (28) simplifies to

$$\gamma_{\text{thrust}} = \frac{St \cdot k}{\Pi_0 \left\{ \left(\frac{f_n}{f}\right)^2 - 1 \right\}} \xrightarrow{f_n \gg f} \frac{St \cdot k}{\Pi_0 \left(\frac{f_n}{f}\right)^2} \sim \frac{St \cdot k}{\Pi_0 \frac{\Pi_1}{\Pi_0}} = \frac{\Pi_0}{\Pi_1} \frac{St \cdot k}{\Pi_0} = \frac{\Pi_0}{\Pi_1} \frac{St \cdot k}{\rho^* h_s^* \left(\frac{k}{\pi}\right)^2}. \tag{29}$$

where the operator ~ indicate proportionality. For a given wing with fixed density ρ_s, thickness h_s, and length, c_m, in a given medium, the density ratio ρ^* and the thickness ratio h_s^* are constant. Then the approximated γ_{thrust} in Eq. (29) further reduces to

$$\gamma_{\text{thrust}} \xrightarrow{f_n \gg f} \frac{\Pi_0}{\Pi_1} \frac{St \cdot k}{\rho^* h_s^* \left(\frac{k}{\pi}\right)^2} \sim \frac{\Pi_0}{\Pi_1} \frac{St \cdot k}{k^2} = \frac{\Pi_0}{\Pi_1} \frac{St}{k} = \frac{\rho_f h_s h_a f^2 c_m^3}{E h_s^3} = \mathcal{N}_{ei}. \tag{30}$$

In the discussion of $\mathcal{N}_{ei}$ Thiria and Godoy-Diana[33] only considers the inertial term arising from the motion of the wing for the forces, which is proportional to $St \cdot k \cdot \rho^* \cdot h_s^*$, see also Appendix G. In that case the term appearing in the denominator in Eq. (30) would cancel out directly. Either way γ_{thrust} is consistent with $\mathcal{N}_{ei}$.

Figure 13 shows that γ_{thrust} is able to scale for the plunging chordwise flexible airfoils in water under freestream at Re = 9.0×10^3 as well as for the flapping isotropic Zimmerman wing in still air at Re = 1.5×10^3 with different motion type and Reynolds number. The time averaged thrust coefficient in the y-axis is normalized with the effective stiffness, Π_1 and St, where the factor St, which for small values is proportional to the effective angle of attack, gives the projection of the resulting force in the vertical direction, i.e. the direction along the displacement w_3. $< C_T/(\Pi_1 \cdot St) >$ can be considered as the static tip deflection: in steady case the tip deflection would be proportional to $< C_T/(\Pi_1 \cdot St) >$. Figure 13 suggests that a correlation exists between the static tip deflection and the maximum tip deformation in the dynamic motion of the wing. A linear fit in least square sense through all data points gives an a priori approximation for the time averaged thrust coefficient as

$$< C_T > \approx 10^{2.26} \cdot \Pi_1 \cdot St \cdot (\gamma_{\text{thrust}})^{1.28}, \tag{31}$$

where the coefficient of determination is 0.97. Eq. (31) can also be used to predict parametric dependence of the thrust on a particular variable. The resonance behavior is not regarded in this study and is part of the on-going studies. For simplicity assume that $f_n \gg f$, then Eq. (31) simplifies to

$$< C_T > \approx 10^{2.26} \cdot \Pi_1 \cdot St \cdot \left(\frac{St \cdot k}{\Pi_1}\right)^{1.28} \sim St^{2.28} \cdot k^{1.28} \cdot \Pi_1^{-0.28}, \tag{32}$$

or, in terms of dimensional variables, the thrust will depend as

$$T \sim f^{3.56} \cdot h_a^{2.28} \cdot c_m^{2.28} \cdot \rho_f^{1.28} \cdot h_s^{-0.84} \cdot E^{-0.28} \cdot U_{\text{ref}}^{-1}. \tag{33}$$

So for a given system the thrust will enhance due to the flexibility, with increasing motion frequency, plunging amplitude, wing length, and fluid density, and with decreasing thickness and Young's modulus of the wing, assuming the motion frequency is sufficiently smaller than the natural frequency of the wing. In forward flight, $U_{\text{ref}} = U_\infty$ and the thrust will decrease with increasing forward speed, while in hovering, $U_{\text{ref}} \sim f h_a$.

IV. Conclusion and Summary

Using a time-domain partitioned fluid-structure interaction solver and surrogate modeling approaches the thrust generation and the degree of the FSI coupling has been investigated for flexible flapping wings under hover and freestream condition. For a flapping isotropic Zimmerman wing in still air at Re = 1.5×10^3 the surrogate models for the time averaged thrust show qualitative similar trends as the twist and the bending angles of the wing. It is not only the effective stiffness, or the density ratio, but the balance between these two parameters that determine the resulting deformation and the thrust generation. Instantaneous thrust peaks are correlated to the flexible-induced bending and twist angles. The twisting of the wing redistributes the resulting force favorable of the mean and instantaneous thrust generation in the direction of the flapping axis.

To further investigate the flexibility induced thrust enhancement a plunging chordwise flexible airfoil in forward flight in water at $Re = 9.0\times10^3$ is considered. Time averaged thrust increases with thinner plate and higher Strouhal number, however the thinnest structure responded with degradation in performance for higher Strouhal numbers.

A unified scaling parameter (FSI shape factor, γ_{FSI}) for the degree of FSI-coupling for the abovementioned cases is proposed based on the properly non-dimensionalized structural dynamic equations. The number of FSI-subiterations is monotonically dependent on γ_{FSI} and it is found that when γ_{FSI} increases, more FSI-subiterations are required, i.e. the system becomes tightly-coupled. This scaling analysis shows that not only the density ratio or the effective stiffness need to be considered to estimate the degree of the FSI-coupling, but also the reduced frequency, the thickness ratios, and the Strouhal number.

Furthermore, a different unified scaling parameter (thrust shape factor, γ_{thrust}) for the time averaged thrust is proposed. The thrust shape factor is related to the maximum tip deformation of the wing and determines the increase of thrust favorable projected area due to the wing flexibility: The thrust normalized by the effective stiffness for both cases scales with the maximum tip deformation. Hence, this scaling analysis suggests that there is a correlation between the static tip deflection and the dynamic tip deformation. The two scaling parameters proposed are consistent with the two cases considered regardless of the precise motion kinematics: flapping/plunging, hover/forward flight; Reynolds number: 1.5×10^3/9.0×10^3; medium of the fluid: air/water.

Appendix

A. Spatial and Temporal Sensitivity Analysis of the Isotropic Flapping Zimmerman wing Study in Still Air

For the rigid Zimmerman wing with the baseline reduced frequency $k = 0.56$ the spatial sensitivity has been investigated by comparing the lift and the thrust coefficients on three different grids at $Re = 1.5\times10^3$: Coarse with 3.4×10^5, Baseline with 5.1×10^5, and Fine with 7.4×10^5 cells respectively, see Figure 14. The resulting aerodynamic forces indicate that the baseline grid has grid independent solution. The first grid spacing from the airfoil surface is set to 2.5×10^{-3} c_m to sufficiently capture the boundary layer and the outer boundary of the computational grid is located at 30 chords from the wing. The time step sensitivity is assessed by varying the time step as = 250, 500, and 1000 on the baseline grid. The resulting forces in Figure 15 show that t/dT= 500 is sufficient. For all computations the baseline grid is used with 500 time steps per motion cycle. The flow is assumed to be laminar. Non-slip boundary condition is assigned to the wing surface and incompressible inlet condition is set to outer boundaries.

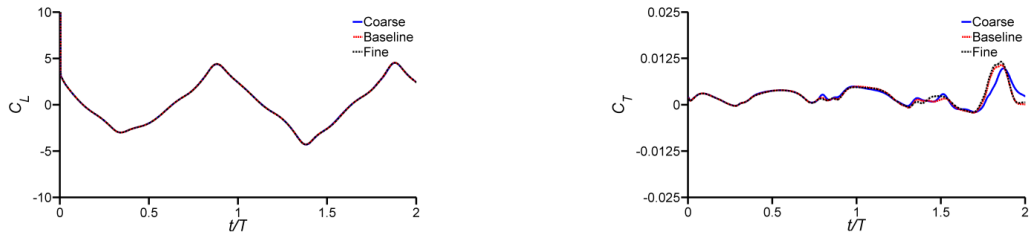

(a) Lift **(b) Thrust**

Figure 14. (a) Lift and (b) thrust coefficients of a flapping Zimmerman wing at $Re = 1.5\times10^3$ and $k = 0.56$ on the Coarse (3.4×10^5 cells), Baseline (5.1×10^5 cells), and Fine (7.4×10^5 cells) grids using 500 time steps per motion cycle.

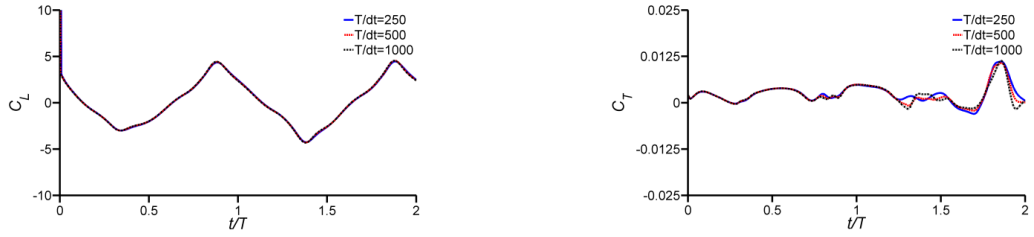

(a) Lift **(b) Thrust**

Figure 15. (a) Lift and (b) thrust coefficients of a flapping Zimmerman wing at $Re = 1.5\times10^3$ and $k = 0.56$ the baseline grid using 250, 500, and 1000 time steps per motion cycle.

B. Design Space for Surrogate Modeling

Table 5 shows the list of training points in the design space for the flapping isotropic Zimmerman wing at $\boldsymbol{Re}$= 1.5×10^3, $\boldsymbol{k}$ = 0.56 in still air. $\boldsymbol{\Pi_1}$ and $\boldsymbol{\rho^*}$ are the design variables. The Young's moduli and the wing material density are shown for reference.

Table 5. List of training points in the design space for the flapping isotropic Zimmerman wing at Re=1.5×10^3 and k = 0.56 in still air. Π_1 and ρ^* are the design variables.

Case Number	Π_1	ρ^*	E	ρ_s
1	1.04×10^2	1.00×10^1	2.00×10^8	1.23×10^1
2	1.04×10^5	1.00×10^1	2.00×10^{11}	1.23×10^1
3	1.04×10^5	1.00×10^4	2.00×10^{11}	1.23×10^4
4	1.00×10^3	1.00×10^3	1.92×10^9	1.23×10^3
5	3.29×10^3	3.16×10^2	6.32×10^9	3.89×10^2
6	1.04×10^5	3.16×10^2	2.00×10^{11}	3.89×10^2
7	3.29×10^3	1.00×10^1	6.32×10^9	1.23×10^1
8	4.38×10^4	2.19×10^3	8.41×10^{10}	2.69×10^3
9	1.00×10^4	1.00×10^2	1.92×10^{10}	1.23×10^2
10	3.16×10^2	3.16×10^1	6.07×10^8	3.89×10^1
11	5.86×10^2	3.06×10^2	1.13×10^9	3.77×10^2
12	3.78×10^3	5.72×10^1	7.26×10^9	7.04×10^1

C. Modal Analysis of Flapping Isotropic Zimmerman Wing Studies

Natural frequencies are computed using MSC.Marc[22] and shown in Table 6. Moreover, the mode shapes of the wing for each natural frequency are illustrated in Figure 16.

Table 6. First four natural frequencies based on a modal analysis for the training and testing points in the design space for flapping isotropic Zimmerman wings at Re=1.5×10^3 and k = 0.56 in still air.

Case	Mode 1	Mode 2	Mode 3	Mode 4
1	7.46×10^1	3.04×10^2	5.27×10^2	7.63×10^2
2	2.36×10^3	9.61×10^3	1.67×10^4	2.41×10^4
3	7.46×10^1	3.04×10^2	5.27×10^2	7.63×10^2
4	2.31×10^1	9.41×10^1	1.63×10^2	2.36×10^2
5	7.46×10^1	3.04×10^2	5.27×10^2	7.63×10^2
6	4.19×10^2	1.71×10^3	2.96×10^3	4.29×10^3
7	4.19×10^2	1.71×10^3	2.96×10^3	4.29×10^3
8	1.03×10^2	4.21×10^2	7.30×10^2	1.06×10^3
9	2.31×10^2	9.41×10^2	1.63×10^3	2.36×10^3
10	7.31×10^1	2.98×10^2	5.16×10^2	7.47×10^2
11	3.20×10^1	1.31×10^2	2.26×10^2	3.27×10^2
12	1.88×10^2	7.65×10^2	1.33×10^3	1.92×10^3

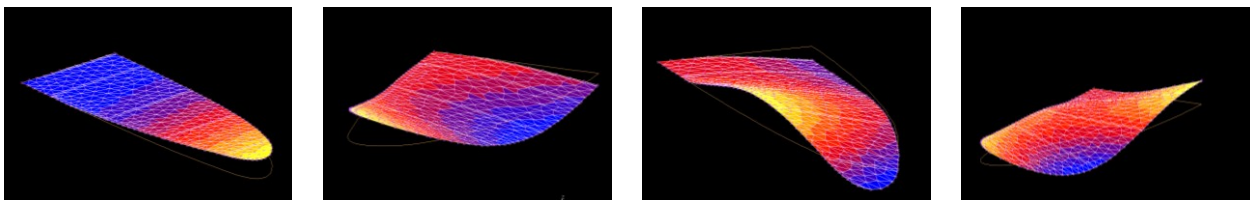

Mode 1 Mode 2 Mode 3 Mode 4

Figure 16. Snapshots of the wing shapes for the first four modes based on a modal analysis for the training and testing points in the design space for the flapping isotropic Zimmerman wing at Re=1.5×10^3 and k = 0.56 in still air.

D. Surrogate Model Characteristics

Table 7. Acronyms and descriptions of the surrogate models used to construct the WAS.

Surrogate model	Model/kernel	Comment
KRG: Kriging	Linear Regression Model	Gaussian correlation model
PRS: Polynomial Response Surface	2nd order polynomial	
SVR1: Support Vector Regression	Linear spline kernel	Full: infinity as upper bound
SVR2: Support Vector Regression	Linear spline kernel	Short: finite upper bound
SVR3: Support Vector Regression	Exponential kernel	Full
SVR4: Support Vector Regression	Exponential kernel	Short
SVR5: Support Vector Regression	Gaussian kernel	Full
SVR6: Support Vector Regression	Gaussian kernel	Short

E. Independent Testing Point Error Measures

Table 8 Relative error of the constructed weighted averaged surrogate at independent testing points for the objective functions considered.

Objective function	relative error at testing point 11 (%)	relative error at testing point 12 (%)
$< C_T >$	41	9.9
twist	36	12
bending	36	9.0
$< N_{\mathrm{FSI}} >$	12	19

F. Tabulation of Results for the Chordwise Flexible Airfoil and Isotropic Wing cases

Table 9. Tabulation of the time averaged number of FSI-subiterations, time averaged thrust coefficient, density ratio, thickness ratio, Strouhal number, effective stiffness, and effective inertia for all cases.

	$< N_{\mathrm{FSI}} >$	$< C_T >$	ρ^*	h_s^*	St	Π_0	Π_1
Chordwise inflexible	2.9	-0.0087	0.78×10^{1}	4.23×10^{-3}	0.075	4.90×10^{-3}	1.3×10^{2}
Chordwise inflexible	3.0	0.25	0.78×10^{1}	4.23×10^{-3}	0.15	1.97×10^{-2}	1.3×10^{2}
Chordwise inflexible	3.4	1.51	0.78×10^{1}	4.23×10^{-3}	0.25	5.48×10^{-2}	1.3×10^{2}
Chordwise inflexible	3.9	4.59	0.78×10^{1}	4.23×10^{-3}	0.4	1.40×10^{-1}	1.3×10^{2}
Chordwise flexible	4.8	-0.0048	0.78×10^{1}	1.41×10^{-3}	0.075	1.60×10^{-3}	4.8×10^{0}
Chordwise flexible	5.0	0.32	0.78×10^{1}	1.41×10^{-3}	0.15	6.60×10^{-3}	4.8×10^{0}
Chordwise flexible	6.2	2.33	0.78×10^{1}	1.41×10^{-3}	0.25	1.83×10^{-2}	4.8×10^{0}
Chordwise flexible	6.8	9.38	0.78×10^{1}	1.41×10^{-3}	0.4	4.68×10^{-2}	4.8×10^{0}
Chordwise very flexible	7.7	0.039	0.78×10^{1}	0.56×10^{-3}	0.075	6.53×10^{-4}	3.0×10^{-1}
Chordwise very flexible	10.9	0.80	0.78×10^{1}	0.56×10^{-3}	0.15	2.60×10^{-3}	3.0×10^{-1}
Chordwise very flexible	11.5	1.81	0.78×10^{1}	0.56×10^{-3}	0.25	7.30×10^{-3}	3.0×10^{-1}
Chordwise very flexible	12.4	3.67	0.78×10^{1}	0.56×10^{-3}	0.4	1.86×10^{-3}	3.0×10^{-1}
Isotropic wing: case 1	5.0	0.058	1.00×10^{1}	2.00×10^{-2}	0.25	6.49×10^{-3}	1.04×10^{2}
Isotropic wing: case 2	2.0	0.0067	1.00×10^{1}	2.00×10^{-2}	0.25	6.49×10^{-3}	1.04×10^{5}
Isotropic wing: case 3	2.0	0.014	1.00×10^{4}	2.00×10^{-2}	0.25	6.49×10^{0}	1.04×10^{5}
Isotropic wing: case 4	2.0	0.12	1.00×10^{3}	2.00×10^{-2}	0.25	6.49×10^{-1}	1.0×10^{3}
Isotropic wing: case 5	2.0	0.01	3.16×10^{2}	2.00×10^{-2}	0.25	2.05×10^{-1}	3.29×10^{3}
Isotropic wing: case 6	2.0	0.0069	3.16×10^{2}	2.00×10^{-2}	0.25	2.05×10^{-1}	1.04×10^{5}
Isotropic wing: case 7	3.0	0.0083	1.00×10^{1}	2.00×10^{-2}	0.25	6.49×10^{-3}	3.29×10^{3}
Isotropic wing: case 8	2.0	0.0080	2.19×10^{3}	2.00×10^{-2}	0.25	1.42×10^{1}	4.38×10^{4}
Isotropic wing: case 9	2.0	0.0079	1.00×10^{2}	2.00×10^{-2}	0.25	6.49×10^{-2}	1.0×10^{4}
Isotropic wing: case 10	4.0	0.029	3.16×10^{1}	2.00×10^{-2}	0.25	2.05×10^{-2}	3.16×10^{2}
Isotropic wing: case 11	2.0	0.027	3.06×10^{2}	2.00×10^{-2}	0.25	1.99×10^{-1}	5.86×10^{2}
Isotropic wing: case 12	2.0	0.0091	5.72×10^{1}	2.00×10^{-2}	0.25	3.71×10^{-2}	3.78×10^{3}

G. Solution of the Normalized Beam Equation

Imposing a plunging motion for the root displacement of a beam leads to a partial differential equation (PDE) with time-dependent boundary conditions. Mindlin and Goodman[51] suggested a procedure to solve a class of beam-vibration problems with time-dependent boundary conditions by extending the method of separation of variables. The governing equation, Eq. (12), for a plunging beam with its boundary condition where the plunging motion given by Eq. (14), and initial condition are, simplifying the fluid force as the lift due to added mass effect for a sinusoidally plunging thin flat plate[50],

$$\textbf{GE}: \Pi_0 \frac{\partial^2 w_3^*}{\partial t^{*2}} + \Pi_1 \frac{\partial^4 w_3^*}{\partial x_1^{*4}} = 2\pi^2 \cdot St \cdot k \cdot \cos(2\pi t^*),$$

$$\textbf{BC}: w_3^*(0,t^*) = f(t^*) = \frac{St\cdot\pi}{k}\{\cos(2\pi t^*) - 1\},\ \frac{\partial w_3^*(0,t^*)}{\partial x_1^*} = 0,\ \frac{\partial^2 w_3^*(1,t^*)}{\partial x_1^{*2}} = 0,\ \frac{\partial^3 w_3^*(1,t^*)}{\partial x_1^{*3}} = 0,$$

$$\textbf{IC}: w_3^*(x_1^*,0) = \frac{St\cdot\pi}{k},\ \frac{\partial w_3^*(x_1^*,0)}{\partial t^*} = 0,$$

where the spatial variable is defined between the root and the tip, i.e. $0 \le x_1^* \le 1$, and the time $t^* \ge 0$, and the effective inertia, again, $\Pi_0 = \rho^* h_s^* \left(\frac{k}{\pi}\right)^2$. For the force term For simplicity the $(\cdot)^*$ notation to denote non-dimensionalized variables and the indices will be omitted: $x = x_1^*$, $t = t^*$, and $w = w_3^*$.

Following the procedure described by Mindlin and Goodman[51], a PDE with homogeneous boundary conditions can be found by looking for the solutions in the form of:

$$w(x,t) = u(x,t) + f(t)\xi(x)$$

where $\xi(x)$ needs to be chosen to make the governing equation for $w(x,t)$ homogeneous. For a sinusoidal plunging motion the unit help function suffices, i.e. $\xi(x) = 1$, so that the governing equation and the corresponding boundary and initial conditions become

$$\Pi_0 \frac{\partial^2 u}{\partial t^2} + \Pi_1 \frac{\partial^4 u}{\partial x^4} = 2\pi^2 \cdot St \cdot k \cdot \cos(2\pi t) - \Pi_0 \frac{d^2 f(t)}{dt^2}$$

$$u(0,t) = 0, \qquad \frac{\partial u(0,t)}{\partial x} = 0, \qquad \frac{\partial^2 u(1,t)}{\partial x^2} = 0, \qquad \frac{\partial^3 u(1,t)}{\partial x^3} = 0,$$

$$u(x,0) = 0, \qquad \frac{\partial u(x,0)}{\partial t} = 0.$$

The consequence of having a sinusoidal displacement at the root is that the vibrational response of the beam is equivalent as having a sinusoidal excitation force. Combined with the force due to fluid force the RHS of Eq. (22), let's say $g(t)$, simplifies to

$$\Pi_0 g(t) = 2\pi^2 \cdot St \cdot k \cdot \cos(2\pi t) - \Pi_0 \frac{d^2 f(t)}{dt^2} = 2\pi^2(1 + 2\pi\rho^* h_s^*) \cdot St \cdot k \cdot \cos(2\pi t).$$

This PDE can be solved using the method of separation, i.e. $u(x,t) = X(x)T(t)$, resulting in

$$\frac{d^4 X}{dx^4} - k_n^4 X = 0,$$

$$\frac{d^2 T}{dt^2} + \omega_n^2 T = Q_n g(t),$$

where $Q_n(t)$ is a Fourier coefficient of a unit function in the spatial modes X_n. So,

$$\sum_{n=1}^{\infty} Q_n X_n = 1,$$

$$Q_n = \frac{\int_0^l X_n dx}{\int_0^l X_n^2 dx},$$

where we have used the orthogonality of X_n.

The equation and the boundary conditions for $X(x)$ is the same as for a free vibrating cantilever beam, of which the solution is given numerous textbooks, ex. by Timoshenko *et al.*[52]. The natural frequency is given by

$$\omega_n^2 = \frac{k_n^4}{1^4}\frac{\Pi_1}{\Pi_0} = \left(\frac{2\pi f_n}{f}\right)^2,$$

where f_n is the natural frequency of the beam, i.e.,

$$(2\pi f_n)^2 = \frac{(k_n L)^4}{L^4}\frac{E h_s^2}{\rho_s},$$

where L is the length of the beam, ex. the chord of a chordwise flexible airfoil, or the half span of a wing, f is the imposed motion frequency at the root, and k_n is the eigenvalue belonging to the spatial mode X_n that satisfies

$$\cos(k_n L)\cosh(k_n L) = -1,$$

and can be approximated the formula

$$k_n L \approx \left(n + \frac{1}{2}\right)\pi,$$

and finally the spatial modes are given by

$$X(x) = -\frac{1}{2}\left[\{\cos(k_n x) - \cosh(k_n x)\} - \frac{\cos(k_n) + \cosh(k_n)}{\sin(k_n) + \sinh(k_n)}\{\sin(k_n x) - \sinh(k_n x)\}\right].$$

The initial position of the beam is consistent with the imposed boundary condition. The solution for the temporal equation in $T(t)$ is

$$T(t) = \frac{2\pi(1 + 2\pi\rho^* h_s^*)\cdot St \cdot k \cdot Q_n}{\Pi_0(f_n^2/f^2 - 1)}\{\cos(2\pi t) - \cos(\omega_n t)\},$$

which means that there is an amplification factor of $1/(\omega_n^2/(2\pi f)^2 - 1) = 1/(f_n^2/f^2 - 1)$ depending on the ratio between the natural frequency f_n of the beam and the excitation frequency f. A caution should be made that this analysis assumes a simple uncoupled linearized estimation for the fluid force on the structure accounting for the added mass effects only.

The full solution is

$$w(x,t) = \frac{St \cdot \pi}{k}\cos(2\pi t) + \sum_{n=1}^{\infty}\frac{2\pi(1 + 2\pi\rho^* h_s^*)\cdot St \cdot k \cdot Q_n}{\Pi_0(f_n^2/f^2 - 1)}\{\cos(2\pi t) - \cos(\omega_n t)\}\left[\{\cos(k_n x) - \cosh(k_n x)\} - \frac{\cos(k_n) + \cosh(k_n)}{\sin(k_n) + \sinh(k_n)}\{\sin(k_n x) - \sinh(k_n x)\}\right].$$

Acknowledgments

The work supported here has been supported in part by the Air Force Office of Scientific Research's Multidisciplinary University Research Initiative (MURI) grant and by the Michigan/AFRL (Air Force Research Laboratory)/Boeing Collaborative Center in Aeronautical Sciences.

References

1. http://www.engineering.utoronto.ca/About/Engineering_in_the_News/Human-powered_Ornithopter_Becomes_First_Ever_to_Achieve_Sustained_Flight.htm
2. Muller, T. J. (ed.), *Fixed and Flapping Wing Aerodynamics for Micro Air Vehicle Applications,* AIAA Prog Astronaut Aeronaut, AIAA, New York, 2002, 195.
3. Shyy, W., Lian, Y., Tang, J., Viieru, D., and Liu, H., *Aerodynamics of Low Reynolds Number Flyers,* Cambridge University Press, New York, 2008.
4. Shyy, W., Berg, M., and Ljungqvist, D., "Flapping and Flexible Wings for Biological and Micro Air Vehicles," *Progress in Aerospace Sciences*, Vol. 24, No. 5, 1999, pp. 455-505.
doi: 10.1016/S0376-0421(98)00016-5
5. Floreano, D., Zufferey, J-C., Srinivasan, M., and Ellington, C. (ed.), *Flying Insects and Robots*, Springer-Verlag, Berlin, Germany, 2009.
6. Combes, S. A., and Daniel, T. L., "Flexural Stiffness in Insect Wings I. Scaling and the Influence of Wing Venation," *Journal of Experimental Biology*, Vol. 206, pp. 2979-2987, 2003
doi: 10.1242/jeb.00523
7. Heathcote, S., and Gursul, I., "Flexible Flapping Airfoil Propulsion at Low Reynolds Numbers," *AIAA* Journal, Vol. 45, No. 5, 2007, pp.1066–79.
doi: 10.2514/1.25431
8. Zhao, L., Huang, Q., Deng, X., and Sane, S., "Aerodynamic Effects of Flexibility in Flapping Wings," *Journal of the Royal Society Interface*, Vol. 7. No. 44, 2010, pp. 485-497.
doi:10.1098/rsif.2009.0200.
9. Katz, J. and Weihs, D., "Hydrodynamic Propulsion by Large Amplitude Oscillation of an Airfoil with Chordwise Flexibility," *Journal of Fluid Mechanics*, Vol. 88, No. 3, 1978, pp. 485–97.
doi: 10.1017/S0022112078002220
10. Shyy, W., Aono, H., Chimakurthi, S.K., Trizila, P., Kang, C., Cesnik, C.E.S., and Liu, H., "Recent Progress in Flapping Wing Aerodynamics and Aeroelasticity," *Progress in Aerospace Sciences*, Vol. 46, No. 7, 2010, pp. 284-327 .
doi: 10.1016/j.paerosci.2010.01.001
11. Ishihara, D., Horie, T., and Denda, M., "A Two-dimensional Computational Study on the Fluid-Structure Interaction Cause of Wing Pitch Changes in Dipteran Flapping Wing," *The Journal of Experimental Biology*, Vol. 212, 2009, pp. 3882-3891.
doi: 10.1242/jeb.020404
12. Gopalakrishnan, P., and Tafti, D. K, "Effect of Wing Flexibility on Lift and Thrust Production in Flapping Flight," *AIAA Journal*, Vol. 48, No. 5, 2010, pp. 865-877.
doi: 10.2514/1.39957
13. Heathcote, S., Wang, Z., and Gursul, I., "Effect of Spanwise Flexibility on Flapping Wing Propulsion," *Journal of Fluid and Structures*, Vol. 24, No.2, 2008, pp. 183-199.
doi: 10.1016/j.jfluidstructs.2007.08.003
14. Chimakurthi, S. K., Tang, J., Palacios, R., Cesnik, C. E. S., and Shyy W., "Computational Aeroelasticity Framework for Analyzing Flapping Wing Micro Air Vehicles," *AIAA Journal*, Vol. 47, No. 8, 2009, pp. 1865-1878.
doi: 10.2514/1.38845
15. Aono, H., Chimakurthi, S.K., Cesnik, C.E.S., Liu, H., and Shyy, W., "Computational Modeling of Spanwise Effects on Flapping Wing Aerodynamics," AIAA 2009-1270.
16. Zhu, Q., "Numerical Simulation of a Flapping Foil with Chordwise or Spanwise Flexibility," *AIAA Journal*, Vol. 45, No. 10, 2007, pp. 2448-2457.
doi: 10.2514/1.28565
17. Eldredge, J. D., Toomey, J., and Medina, A., "On the Roles of Chord-wise Flexibility in a Flapping Wing with Hovering Kinematics," *Journal of Fluid Mechanics*, Vol. 659, 2010, pp. 94-115.
doi: 10.1017/S0022112010002363

18. Tang, J., Chimakurthi, S. K., Palacios, R., Cesnik, C. E. S., and Shyy, W., "Computational Fluid-Structure Interaction of a Deformable Flapping Wing for Micro Air Vehicle Applications," AIAA 2008-615.
19. Chimakurthi, S. K., Stanford, B. K., Cesnik, C. E. S., and Shyy, W., "Flapping Wing CFD/CSD Aeroelastic Formulation Based on a Co-rotational Shell Finite Element," AIAA 2009-2412.
20. Aono, H., Chimakurthi, S. K., Wu, P., Sällström, E., Stanford, B. K., Cesnik, C. E. S., Ifju, P., Ukeiley, L, and Shyy, W., "A Computational and Experimental Study of Flexible Flapping Wing Aerodynamics," AIAA 2010-554.
21. Aono, H., Kang, C., Cesnik, C. E. S., and Shyy, W., "A Numerical Framework for Isotropic and Anisotropic Flexible Flapping Wing Aerodynamics and Aeroelasticity," AIAA 2010-5082.
22. *MSC.Marc Documentation Volumes A-E*, MSC. Software Corporation, Santa Ana, California, 2005.
23. Gordnier, R.E., Attar P.J., Chimakurthi, S. K., and Cesnik, C. E. S., "Implicit LES Simulations of a Flexible Flapping Wing," AIAA 2010-2060.
24. McClung, A., Stanford, B., and Beran, P, "High-Fidelity Models for the Fluid-Structure Interaction of a Flexible Heaving Airfoil," AIAA 2010-2959.
25. Stanford, B., Kurdi, M., Beran, P., and McClung, A., "Shape-Structure, and Kinematic Parameterization of a Power-Optimal Hovering Wing," AIAA 2010-2963.
26. Gogulapati, A., Friedmann, P. P., Kheng, E., and Shyy, W., "Approximate Aeroelastic Modeling of Flapping Wings: Comparison with CFD and Experimental Data," AIAA 2010-2707.
27. Causin, P., Gerbeau, J. F., and Nobile, F., "Added-mass Effect in the Design of Partitioned Algorithms for Fluid-Structure Problems," *Computational Methods in Applied Mechanical Engineering*, Vol. 194, 2005, pp. 4506-4527.
doi: 10.1016/j.cma.2004.12.005
28. Küttler, U., and Wall, W. A., "Fixed-point Fluid-structure Interaction Solvers with Dynamic Relaxation," *Computational Mechanics*, Vol. 43, No.1 2008, pp. 61-72.
doi: 10.1007/s00466-008-0255-5
29. Küttler, U., and Wall, W. A., "Vector Extrapolation for Strong Coupling Fluid-Structure Interaction Solvers," *Journal of Applied Mechanics*, Vol. 76, 2009, pp.1-7.
doi: 10.1115/1.3057468
30. Minami, S., and Yoshimura, S., "Performance Evaluation of Nonlinear Algorithms with Line-Search for Partitioned Coupling Techniques for Fluid-structure Interactions," *International Journal for Numerical Methods in Fluids*, Vol. 64, 2010, pp. 1129-1147.
doi: 10.1002/fld.2274
31. Anderson, J. D., *Fundamentals of Aerodynamics*, 2nd ed., McGraw Hill Higher Education, Singapore, 1991.
32. Lentink, D., and Dickinson, M. H., "Biofluiddynamic Scaling of Flapping, Spinning and Translating Fins and Wings," *The Journal of Experimental Biology*, Vol. 212, 2009, pp. 2691-2704.
doi: 10.1242/jeb.022251
33. Thiria, B., and Godoy-Diana, R., "How Wing Compliance Drives the Efficiency of Self-propelled Flapping Flyers," *Physical Review E*, Vol. 82, 2010, 015303, pp. 1-4.
doi: 10.1103/PhysRevE.82.015303
34. de Boer, A., van der Schoot, M. S., and Bijl, H., "Mesh Deformation Based on Radial Basis Function Interpolation," *Computers and Structures*, Vol. 85, 2007, pp. 784-795.
doi: 10.1016/j.compstruc.2007.01.013
35. Cho, Y., Jayaraman, B., Viana, F. A. C., Hafka, R.T., and Shyy, W., "Surrogate Modeling for Characterizing the Performance of Dielectric Barrier Discharge Plasma Actuator," AIAA 2008-1381.
36. Zhang, X., Sastry, A.M., and Shyy, W., "Intercalation-Induced Stress and Heat Generation within Single Lithium-Ion Battery Cathode Particles," *Journal of The Electrochemical Society*, Vol. 155, No. 5, 2008, pp. 542-552.
doi: 10.1149/1.2926617
37. Trizila, P, Kang, C., Visbal, M., and Shyy, W., "A Surrogate Model Approach in 2D versus 3D Flapping Wing Aerodynamic Analysis," AIAA 2008-5914.
38. Wright, J. A., and Smith, R. W., "An Edge-Based Method for the Incompressible Navier-Stokes Equations on Polygonal Meshes," *Journal of Computational Physics*, Vol. 169, 2001, pp. 24-43.
doi: 10.1006/jcph.2001.6705
39. Smith, R.W., and Wright, J.A., "An Implicit Edge-Based ALE Method for the Incompressible Navier-Stokes Equations," *Intertional Journal for Numererical Methods in Fluids*, Vol 43, 2003, pp.253-279.
doi: 10.1002/fld.606

40. Luke, E. A., and George, T., "Loci: a rule-based framework for parallel multi-disciplinary simulation synthesis," *Journal of Functional Programming*, Vol. 15, Nr. 3, 2005, pp.477-502.
doi: 10.1017/S0956796805005514
41. Shyy, W., "A Study of Finite Difference Approximations to Steady-State, Convection-Dominated Flow Problems", *Journal of Computational Physics*, Vol. 57, No. 3, 1985, pp. 415-438.
doi: 10.1016/0021-9991(85)90188-3
42. Shyy, W., *Computational Modeling for Fluid Flow and Interfacial Transport*, Elsevier, Amsterdam, 1994.
43. Blazek, J., *Computational Fluid Dynamics: Principles and Applications*, Elsevier, Amsterdam, 2001.
44. Balay, S., Buschelman, K., Gropp, W. D., Kaushik, D., Knepley, M. G., McInnes, L. C., Smith, B. F., and Zhang, H, "PETSc Web page", http://www.mcs.anl.gov/petsc, 2009.
45. Falgout, R. D., Jones, J. E., Yang, U. M., 2006. The Design and Implementation of Hypre, a Library of Parallel High Performance Preconditioners. Numerical Solution of Partial Differential Equations on Parallel Computers. Springer-Verlag, pp. 267–294.; also http://www.llnl.gov/CASC/linear solvers/.
46. Thomas, P. D., and Lombard, K., "The Geometric Conservation Law – A Link between Finite-Difference and Finite-Volume Methods of Flow Computation on Moving Grids", AIAA 1978-1208.
47. Kamakoti, R., and Shyy, W., "Evaluation of Geometric Conservation Law using Pressure-Based Fluid Solver and Moving Grid Technique," *International Journal of Numerical Methods for Heat & Fluid Flow*, Vol. 14, No. 7, 2006, pp. 851-865.
doi: 10.1108/09615530410546254
48. Khosravi, P., Ganesan, R., and Sedaghati, R., "Co-rotational Non-linear Analysis of Thin Plates and Shells Using a New Shell Element," *International Journal for Numerical Methods in Fluids*, Vol. 69, 2007, pp. 859-885.
doi: 10.1002/nme.1791
49. Wu, P., and Ifju, P., "Micro Air Vehicle Flapping Wing Effectiveness, Efficiency, and Aeroelasticity Relationships," AIAA 2010-1017.
50. Theodorsen, T., "General Theory of Aerodynamic Instability and the Mechanism of Flutter," *N.A.C.A. Report* 496, 1935.
51. Mindlin, R. D., and Goodman, L. E., "Beam Vibrations with Time-dependent Boundary Conditions," *Journal of Applied Mechanics*, Vol. 17, 1950, pp. 377 – 380.
52. Timoshenko, S., Young, D. H., and Weaver, J. R., W., *Vibration Problems in Engineering*, John Wiley & Sons, New York, 1974.